CO and [CII] line emission of molecular clouds – the impact of stellar feedback and non-equilibrium chemistry

S. Ebagezio,[1]★ D. Seifried,[1] S. Walch,[1] P. C. Nürnberger,[1] T.-E. Rathjen,[1,2] T. Naab[2]
[1]Universität zu Köln, I. Physikalisches Institut, Zülpicher Str. 77, 50937 Köln, Germany
[2]Max Planck Institute for Astrophysics, Karl-Schwarzschild-Str. 1, 85748 Garching, Germany

Accepted XXX. Received YYY; in original form ZZZ

ABSTRACT

We analyse synthetic ^{12}CO, ^{13}CO, and [CII] emission maps of simulated molecular clouds of the SILCC-Zoom project, which include an on-the-fly evolution of H_2, CO, and C^+ chemistry. We use simulations of hydrodynamical and magnetohydrodynamical clouds, both with and without stellar feedback. We introduce a novel post-processing of the C^+ abundance using Cloudy, necessary in HII regions to account for further ionization states of carbon due to stellar radiation. With this post-processing routine, we report the first self-consistent synthetic emission maps of [CII] in feedback bubbles. The bubbles are largely devoid of emission inside them, as recently found in observations. The C^+ mass is only poorly affected by stellar feedback but the [CII] luminosity increases by 50 – 85 per cent compared to reference runs without feedback due to the increase of the excitation temperature. Furthermore, we show that, for both ^{12}CO and ^{13}CO, the luminosity ratio, $L_{CO}/L_{[CII]}$, averaged over the entire cloud, does not show a clear trend and can therefore *not* be used as a reliable measure of the H_2 mass fraction or the evolutionary stage of clouds. We note a monotonic relation between $I_{CO}/I_{[CII]}$ ratio and the H_2 fraction for individual pixels of our synthetic maps, but with a too large scatter to reliably infer the fraction of H_2. Finally, we show that assuming chemical equilibrium results in an overestimation of H_2 and CO masses by up to 110 and 30 per cent, respectively, and in an underestimation of H and C^+ masses by 65 and 7 per cent, respectively. In consequence, L_{CO} would be overestimated by up to 50 per cent, and $L_{C[II]}$ be underestimated by up to 35 per cent. Hence, the assumption of chemical equilibrium in molecular cloud simulations introduces intrinsic errors of a factor of up to ~ 2 in chemical abundances, luminosities and luminosity ratios.

Key words: ISM: molecules – radiative transfer – methods: numerical – ISM: clouds – ISM: HII regions – astrochemistry

1 INTRODUCTION

Molecular clouds (MCs) are defined as those regions of the interstellar medium (ISM) where hydrogen exists predominantly in molecular form, H_2. Due to its vanishing dipole moment and low temperatures, typically of a few 10 K, H_2 is not directly observable in MCs. Nevertheless, information on the abundance and distribution of H_2 are of great importance because they allow us to identify the star formation sites in MCs. H_2 is observed only indirectly by means of molecules which trace its presence. The most used molecule to trace H_2 in MCs is CO (e.g. Wilson et al. 1970; Scoville & Solomon 1975; Larson 1981; Solomon et al. 1987; Dame et al. 2001; Bolatto et al. 2013; Dobbs et al. 2014). In order to infer the amount of H_2 from the observations of CO, a conversion factor X_{CO} from the observed CO luminosity into a H_2 column density has been established (see e.g. Scoville et al. 1987; Dame et al. 1993; Strong & Mattox 1996; Melchior et al. 2000; Lombardi et al. 2006; Nieten et al. 2006; Smith et al. 2012; Ripple et al. 2013; Bolatto et al. 2013). The standard value of X_{CO} in the Milky Way is commonly assumed to be $X_{CO} = 2 \times 10^{20}$ cm^{-2} K^{-1} km^{-1} s, but there is plenty of evidence that the actual value strongly depends on the environmental conditions (Glover & Mac Low 2011; Shetty et al. 2011a; Bolatto et al. 2013; Gong et al. 2020; Seifried et al. 2020). Furthermore, because of this strong dependence, it is used to assess the total amount of H_2 in a cloud, but it cannot easily used on sub-pc scales (e.g. Bisbas et al. 2021). More in general, CO is not a perfect tracer for H_2 because of (i) the presence of CO-dark areas, which do contain a significant amount of H_2, but almost no CO (see for instance Lada & Blitz 1988; van Dishoeck & Black 1988; Grenier et al. 2005; Glover & Mac Low 2011; Glover & Clark 2016; Seifried et al. 2020), and (ii) the optical thickness of CO in the densest regions, which break the quantitative relation between the CO luminosity and the H_2 amount (e.g. Seifried et al. 2020; Bisbas et al. 2021).

Other chemical species are also used to assess the H_2 abundance in the clouds: neutral carbon emission has been studied in this sense, and the X_C-factor (Papadopoulos et al. 2004; Offner et al. 2014), defined in the same way as X_{CO}, has been used to assess the abundance of H_2 in MCs. The value of X_C, however, also depends on the different environments (Offner et al. 2014; Bisbas et al. 2021). C^+ is another carbon-bearing species which has been studied intensively in MCs and is one of the main coolants of the ISM (Tielens & Hollenbach 1985; Stacey et al. 1991; Ossenkopf et al. 2013; Appleton et al. 2013; Lesaffre et al. 2013; Beuther et al. 2014; Pineda et al. 2013, 2014; Klessen & Glover 2016, and many more). It is most abundant in photo-dissociation regions (Ossenkopf et al. 2013) and in shock fronts (Appleton et al. 2013; Lesaffre et al. 2013). Some studies

★ E-mail: ebagezio@ph1.uni-koeln.de

(e.g. Velusamy & Langer 2014; Franeck et al. 2018) suggest that C^+ is a tracer of some CO-dark areas of the clouds. However, a realiable relation between C^+ emission and H_2 abundance is difficult to establish, because most of the emission comes from regions which are predominantly atomic hydrogen (Franeck et al. 2018).

The formation and evolution of MCs has been studied with numerical simulations in a large number of recent works (e.g. Smith et al. 2014a; Dobbs & Pringle 2013; Ibáñez-Mejía et al. 2016; Gatto et al. 2015; Li et al. 2015; Padoan et al. 2016; Walch et al. 2015; Seifried et al. 2017, and many more). Chemistry treatment is generally performed in two possible ways: one option is to first run the simulations without considering the chemical composition of the clouds and then post-process the chemistry assuming equilibrium (e.g. Gong et al. 2018; Gong et al. 2020; Li et al. 2018; Keating et al. 2020). Post-processing the chemistry enables to use complex networks, but the assumption of equilibrium is necessary and consequences are underestimation of H and overestimation of H_2 abundances (Hu et al. 2021; Borchert et al. 2022; Seifried et al. 2022). Conversely, some other simulations include a treatment of molecule formation with a non-equilibrium chemical network (Clark et al. 2012; Seifried & Walch 2016; Walch et al. 2015; Hu et al. 2016, 2017; Smith et al. 2014b,c, 2020; Hu et al. 2021; Valdivia et al. 2016; Lahén et al. 2020). This usually implies the usage of simpler networks but the assumption of chemical equilibrium is avoided. Recently, non-equilibrium chemistry has been joined with high-resolution simulations up to 0.1 pc. This is computationally demanding and therefore requires large computational resources. This is the case, for instance, in Seifried et al. (2017, 2020); Haid et al. (2019), as part of the SILCC-Zoom project. The simulations presented here serve as a basis of this publication.

In this paper we produce synthetic observations of these simulated MCs using the RADMC-3D radiative transfer code (Dullemond et al. 2012) in order to investigate the CO/[CII] line ratio as alternative tracer to X_{CO} for H_2 and investigate its applicability as an indicator of MC evolution. We also shed light on the role of the assumption of equilibrium chemistry on the emission of CO and [CII]. This paper is structured as follows: in Section 2 we describe the numerical methods which we use to run the simulations and the radiative transfer calculations. In Section 3 we describe the overall aspect of the simulations, the corresponding synthetic observations, the X_{CO} factor, and the line ratios, considering both the total luminosity and the intensity from single pixels. Then, we discuss our results and we analyse the importance of the equilibrium chemistry in Section 4. Finally, we summarise our results in Section 5.

2 NUMERICAL METHODS

2.1 SILCC-Zoom simulations

The simulated MCs we use in this paper are part of the SILCC-Zoom project (Seifried et al. 2017). The simulations are performed within the SILCC project (see Walch et al. 2015; Girichidis et al. 2016, for details) and make use of the zoom-in technique discussed in Seifried et al. (2017). The simulations are performed with the adaptive mesh refinement code FLASH 4.3 (Fryxell et al. 2000; Dubey et al. 2008) and use, for the hydrodynamics (HD) runs, a solver described in Bouchut et al. (2007); Waagan (2009), which guarantees positive entropy and density. Magnetohydrodynamical (MHD) runs use an entropy-stable solver (Derigs et al. 2016, 2018). We model the chemical evolution of the ISM using a chemical network for H^+, H, H_2, C^+, O, CO, and e^- (Nelson & Langer 1997; Glover & Mac Low 2007a,b; Glover et al. 2010), hereafter NL97, which also follows the thermal evolution of the gas including the most important heating and cooling processes. We assume solar metallicity with elemental abundances of carbon and oxygen relative to hydrogen of 1.4×10^{-4} and 3.16×10^{-4}, respectively (Sembach et al. 2000). The ISM is embedded in an interstellar radiation field (ISRF) of $G_0 = 1.7$ in units of Habing (1968), that is in line with Draine (1978). The cosmic ray ionisation rate (CRIR) is set to 3×10^{-17} s^{-1} with respect to atomic hydrogen. For the magnetized runs, we initialize a magnetic field **B** along the x-direction as

$$B_x = B_{x,0}\sqrt{\rho(z)/\rho_0}\,, \tag{1}$$

where $B_{x,0} = 3\,\mu$G is in accordance to recent observations (e.g. Beck & Wielebinski 2013), $\rho_0 = 9 \times 10^{-24}$ g cm^{-3} (see Walch et al. 2015, for more details), and $\rho(z)$ is the initial Gaussian density distribution, with z being the distance from the galactic midplane.

Up to a time t_0 after the beginning of the simulations, supernovae explosions drive turbulence. The rate at which the supernovae are ejected is based on the Kennicutt – Schmidt relation, relating the disc's surface density (here 10 $M_\odot$ pc^{-2}) with a typical star formation rate surface density. The latter is translated into a supernovae rate by assuming a standard initial mass function. We refer to Walch et al. (2015) and Seifried et al. (2017) and references therein for details. At t_0 supernovae explosions are stopped and local overdensities of molecular gas, i.e., the regions where MCs are about to form, are already visible. We therefore select these "zoom-in" regions and continue the simulations allowing for a resolution up to 0.12 pc in those regions. The typical size of the zoom-in regions is about 100 pc. We consider two purely hydrodynamical clouds, which we refer to as MC1-HD and MC2-HD, and two magnetohydrodynamical clouds, MC1-MHD and MC2-MHD. The HD runs are described in detail in Seifried et al. (2017) and the MHD runs in Seifried et al. (2019). We emphasise that HD and MHD runs refer to different clouds, they are not just the same clouds with/without external magnetic field included. In MHD runs t_0 is larger than in the HD runs due to the slower dynamical evolution of the MHD clouds due to the magnetic fields: it is $t_0 = 11.9$ Myr for HD runs and $t_0 = 16.0$Myr for MHD runs. We also run these 4 clouds with stellar feedback included. We distinguish throughout the text by indicating, for instance, MC1-HD-noFB and MC1-HD-FB for non-feedback and feedback runs, respectively. An overview of the simulations features is given in Table 1. In the feedback runs (see Haid et al. 2019, for a more detailed description), we use sink particles to model the formation and the evolution of stars and, as a consequence, of the radiative stellar feedback. The sinks form when the gas density exceeds 1.1×10^{-20} g cm^{-3}, accrete gas and form stars. Every 120 $M_\odot$ of accreted mass, a massive star between 9 and 120 $M_\odot$ is created following the initial mass function of Salpeter (1955). Furthermore, the gas

Table 1. Overview of the simulations giving the run name, the zoom time t_0, the run type (hydrodynamical, HD, or magnetohydrodynamical, MHD), and stellar feedback

run name	t_0 [Myr]	run type	feedback
MC1-HD-noFB	11.9	HD	no
MC1-HD-FB	11.9	HD	yes
MC2-HD-noFB	11.9	HD	no
MC2-HD-FB	11.9	HD	yes
MC1-MHD-noFB	16.0	MHD	no
MC1-MHD-FB	16.0	MHD	yes
MC2-MHD-noFB	16.0	MHD	no
MC2-MHD-FB	16.0	MHD	yes

surrounding the point of formation of the sink particle has to be in a converging flow, gravitationally bound, Jeans unstable, and in a local gravitational potential minimum. Details on this are provided in Federrath et al. (2010). The radiative feedback relative to each star is treated with TreeRay (Wünsch et al. 2018, 2021). The chemical evolution of all HD clouds, as well as MC1-MHD-noFB and MC2-MHD-noFB, in particular for H_2 and CO, is reported in Seifried et al. (2020).

2.2 Chemistry post-processing

We use RADMC-3D (Dullemond et al. 2012) to obtain synthetic observations of our simulations (see Section 2.4 for the details). We use a pipeline developed by P. C. Nürnberger[1] to convert the FLASH simulation data into RADMC-3D input files and, at the same time, to post-process the simulation data to include further physical and numerical processes: (i) CO freeze-out, (ii) $C^+ \rightarrow C^{2+}$ thermal ionization, (iii) splitting of H_2 into para- and orho-H_2, and (iv) the generation of a microturbulence file.

(i) The CO density after the freeze-out post-processing, $n_{\rm CO,f}$, is obtained from the original density $n_{\rm CO}$ following Glover & Clark (2016) and references therein:

$$n_{\rm CO,f} = n_{\rm CO} \times \frac{k_{\rm cr} + k_{\rm therm}}{k_{\rm cr} + k_{\rm therm} + k_{\rm ads}} \,, \tag{2}$$

where

$$k_{\rm cr} = 5.7 \times 10^4 \times {\rm CRIR} \tag{3}$$

is the CR-induced desorption rate of CO from dust grains,

$$k_{\rm therm} = 1.04 \times 10^{12} \exp\left(-\frac{960\,{\rm K}}{T_{\rm d}}\right) \tag{4}$$

is the thermal desorption rate. Here, $T_{\rm g}$ is the gas temperature and $T_{\rm d}$ is the dust temperature. Furthermore,

$$k_{\rm ads} = 3.44 \times 10^{-18} \sqrt{T_{\rm g}}\,(2n_{\rm H_2} + n_{\rm H}) \tag{5}$$

is the adsorption rate due to collisions between CO and dust grains.
(ii) The $C^+ \rightarrow C^{2+}$ ionization due to collisions induced via thermal motions is implemented following Sutherland & Dopita (1993). In cells with a gas temperature $T_{\rm g} \geq 2 \times 10^4$ K the C^+ density is corrected in order to consider such collisions.
(iii) We distinguish between the two nuclear spin states of H_2, in which the spins of the nuclei are parallel (ortho $-$ H_2) or anti-parallel (para $-$ H_2). These are given following, Rachford et al. (2009), by

$$n({\rm para-H_2}) = \frac{n_{\rm H_2}}{9\,e^{-170.5\,{\rm K}/T_{\rm g}} + 1} \tag{6}$$

and

$$n({\rm ortho-H_2}) = n_{\rm H_2} - n({\rm para-H_2}) \,. \tag{7}$$

If Eq. (6) and (7) yield to an ortho-to-para ratio larger than 3, we force $n({\rm ortho-H_2})/n({\rm para-H_2}) = 3$, with $n({\rm ortho-H_2}) + n({\rm para-H_2}) = n_{\rm H_2}$.
(iv) Microturbulence is also included in our radiative transfer calculations. We assume that the microturbulence broadening is as strong as the thermal broadening. Therefore, with a being the line width, we have $a^2 = a_{\rm therm}^2 + a_{\rm turb}^2$, with

$$a_{\rm therm} = a_{\rm turb} = \sqrt{\frac{2k_B T_{\rm g}}{\mu\, m_{\rm p}}} \,, \tag{8}$$

where k_B is the Boltzmann constant, $\mu = 2.3$ is the assumed mean molecular mass of the gas, and $m_{\rm p}$ is the proton mass.

[1] https://bitbucket.org/pierrenbg/flash-pp-pipeline/src/master/

2.3 Stellar feedback post-processing

The NL97 chemical network does not contain any higher ionized states of carbon than C^+ and the ionisation to C^{2+} described before only accounts for thermal ionisation. Stellar radiation, however, can cause further ionization of carbon (see e.g. Abel et al. 2005): the stars formed in our simulations have masses greater or equal to $9{\rm M}_\odot$ and are therefore O-type or B-type stars. These stars, whose effective temperature equals or exceed 24 000 K, emit photons with energies larger than the second ionization energy of carbon of 24.4 eV. It is therefore necessary to remove C^+ which gets further ionized by this radiation in order to obtain more realistic emission maps of the feedback runs. For this purpose we use a novel approach based on Cloudy which we describe in detail in the following.

2.3.1 *Cloudy database*

We consider 4 parameters provided in the FLASH simulation data: the gas density, $n_{\rm g}$, the gas temperature, $T_{\rm g}$, the energy density of ionising photons, $E_{\rm ion}$ (converted later to a bolometric luminosity, see below), and the star temperature, $T_\star$. In order to avoid to run Cloudy for each simulation cell, we create a database beforehand. To do this, we vary the parameters mentioned above over the range of values found in our simulations, summarized in Table 2. We run one Cloudy model for each possible combination of values, which corresponds to approximately 160 000 models in total.

Cloudy requires for a source of ionising photons its bolometric luminosity, $L_{\rm bol}$, and not $E_{\rm ion}$. Therefore, we convert $E_{\rm ion}$ into $L_{\rm bol}$ as follows. Given a defined spectral luminosity L_ν for a star, $L_{\rm bol}$ is defined as

$$L_{\rm bol} = \int_0^\infty L_\nu d\nu \,. \tag{9}$$

Similarly, we define the ionizing luminosity $L_{\rm ion}$ as the spectral luminosity integrated over the frequencies larger than the ionizing frequency of atomic hydrogen, $\nu_{\rm H} = 13.6\,{\rm eV}/h$, where h is the Planck constant:

$$L_{\rm ion} = \int_{\nu_{\rm H}}^\infty L_\nu d\nu \,. \tag{10}$$

Furthermore, assuming that the emission spectrum of the chosen star (see below how we choose the star) is equal to that of a black body with its temperature $T_\star$, $B_\nu\,(T_\star)$, we have

$$L_{\rm bol} = L_{\rm ion} \frac{\int_0^\infty B_\nu\,(T_\star)\,d\nu}{\int_{\nu_{\rm H}}^\infty B_\nu\,(T_\star)\,d\nu} \,. \tag{11}$$

The energy density of ionising photons, provided in the FLASH simulation data, is related to the ionising luminosity (Eq. 10) via

$$E_{\rm ion} = \frac{1}{c}\,\frac{L_{\rm ion}}{4\pi d^2} \,, \tag{12}$$

with d being the distance between the star and the investigated point neglecting the attenuation by the gas and dust in between them. Therefore, we can convert $E_{\rm ion}$ into $L_{\rm bol}$ via

$$L_{\rm bol} = E_{\rm ion} \times 4\pi d^2 c \times \frac{\int_0^\infty B_\nu\,(T_\star)\,d\nu}{\int_{\nu_{\rm H}}^\infty B_\nu\,(T_\star)\,d\nu} \,. \tag{13}$$

In our Cloudy models we now assume a fixed d of 100 pc. Hence,

Table 2. Parameter range used for Cloudy models. We run one model for each combination of parameters. Steps are equally spaced in log-scale.

Parameter	min	max	# steps
n_g [g cm^{-3}]	10^{-26}	10^{-20}	19
T_g [K]	$10^{1.5}$	$10^{4.5}$	19
$T_\star$ [K]	$10^{3.5}$	$10^{5.5}$	21
E_{ion} [erg cm^{-3}]	10^{-18}	10^{-8}	21

Eq. 13 gives us the luminosity of a *hypothetical* star at a distance of 100 pc which would provide the exactly same value for E_{ion} as the actual star at its real distance due to attenuation by gas and dust in between.

This approach thus limits the parameter range to be covered by the Cloudy database to 4 dimensions without loss of generality.

In addition, the length l of our considered simulation cells, which then are taken as the depth of the PDR in Cloudy, are $l \leq 0.96$ pc. Hence, our choice of $d = 100$ pc assures that $l << d$, that is, the Cloudy models are essentially a plane-parallel PDR which we can then directly map back to the simulation cell.

Cloudy provides the fractional abundance $f_{X,cloudy}$ of the chemical species X with respect to the total hydrogen, i.e., $f_{X,cloudy} = n_{X,cloudy}/n_{H,tot}$, as a function of the distance from the edge of the slab. We are interested in the medium value over the cell, to which the slab corresponds. The length of the (quasi plane-parallel) PDR slab in Cloudy is 0.96 pc. The cells in our simulations, however, have a size of $dx = 0.12, 0.24, 0.48$, and 0.96 pc. Hence, in a next step we average the chemical abundance in the PDR slab from 0 to a depth of dx, i.e. each Cloudy model provides now four values of $f_{X,cloudy}$, one for each cell size. Hence, at this point we have a database covering the full range of relevant physical parameters and possible cell lengths.

2.3.2 *Calculation of the new C^+ abundance*

In a next step we now post-process the RADMC input file concerning C^+, which is used for the radiative transfer (see Section 2.4), on a cell-by-cell basis as follows.

- We check whether $E_{ion} > 0$. If this is not the case, we skip the following points and do not post-process the cell. Otherwise,
- In order to estimate which star contributes most to the flux of ionising photons at the considered cell, we loop over all stars and compute the unattenuated flux F_i from to the i-th star reaching the cell:

$$F_i = L_{bol,i}/4\pi d_i^2 \,. \tag{14}$$

Here, d_i is the *actual* distance between the cell and the i-th star and $L_{bol,i}$ the *actual* bolometric luminosity of the i-th star obtained directly from the simulation data.

- We select the k-th star, with temperature $T_{\star,k}$, for which $F_k = \max(F_i)$. For consistency, we check that $d_k \leq 2d_{min}$, with $d_{min} = \min(d_i)$. This is always the case in the simulations presented in this paper. In the following we assume that star k is solely responsible for all the ionizing photons.
- Next, we take the input values n_g, T_g, $T_{\star,k}$, E_{ion}, and the cell size dx and interpolate the database for $f_{C^+,cloudy}$ created before using LinearNDInterpolator, which is part of Python's NumPy library, to obtain the updated value f_{C+} for the given cell.
- Finally, we replace the original C^+ number density of the cell with $f_{C+} \times n_{H,tot}$, where $n_{H,tot}$ is the total hydrogen nuclei density.

2.4 Radiative transfer

We create synthetic emission maps of ^{12}CO ($1 \rightarrow 0$) at 2600 μm, ^{13}CO ($1 \rightarrow 0$) at 2720 μm, and [CII] at 158 μm for all 8 clouds (see Table 1) at various snapshots for lines of sight (LOS) along the x-, y-, and z-axis. The emission maps have the same resolution as the simulations, i.e. 0.12 pc. The radiative transfer, which is needed to obtain synthetic emission maps of the simulated clouds, is performed using the RADMC-3D software, an open-source, 3D radiative transfer code[2] (Dullemond et al. 2012). We include microturbulence (Eq. 8) and use the Large Velocity Gradient approximation (LVG) (Ossenkopf 1997; Shetty et al. 2011a,b) for calculating the level population. In order to capture the contribution of Doppler-shifted emission, we consider a velocity range of ± 20 km s^{-1}, centred around the selected rest frequency. We divide this range into 201 equally spaced velocity channels, corresponding to a spectral resolution of d$v = 0.2$ km s^{-1}.

Performing the radiative transfer calculations using the LVG approximation means that we do not assume Local Thermal equilibrium (LTE). Therefore, we must specify explicitly the collisional rates for CO and C^+. We take the data from the Leiden Atomic and Molecular DAtabase[3] (LAMDA, Schöier et al. 2005). We consider para-H_2, ortho-H_2, H, and e^-, as collisional partners for C^+, and para-H_2, ortho-H_2, H, and He, for CO. As the rates for CO-He and CO-H collisions are not in the LAMDA database, for this we use the rates from Cecchi-Pestellini et al. (2002) and Walker et al. (2015), respectively. We emphasise that it is essential to include also He and H as collisional partners as it increases the CO luminosity by $\sim 20-30$ per cent (Borchert et al. 2021).

We also consider the Cosmic Microwave Background (CMB) using an isotropic black body emission at 2.725 K. During the following analysis we subtract this background from the emission maps before any other step. Each emission map is centered on a rest frequency ν_0. The corresponding brightness temperature for the CMB is given by

$$T_{B,CMB} = \frac{h\nu_0}{k_B} \frac{1}{e^{h\nu_0/kT} - 1} \,, \tag{15}$$

where h is the Planck constant and $T = 2.725$ K. Considering the CMB background and then subtracting it, has a negligible impact on [CII] emission maps, but it changes the ^{12}CO and ^{13}CO intensity in optically thick areas by up to ~ 20 per cent.

3 RESULTS

3.1 Overview of the simulations

In the following, we refer to the evolution time t_{evol} of the clouds as $t_{evol} = t - t_0$, where t is the time calculated from the very beginning of the SILCC simulation and t_0 is the time when the zoom-in simulation starts.

In Fig. 1 we show in the top row the H_{tot} (i.e. molecular, atomic, and ionized hydrogen), H_2, CO, and C^+ column density of MC1-HD-noFB at an evolutionary stage of $t_{evol} = 4$ Myr along the z-axis. In the bottom row we show MC1-HD-FB together with the formed stars. The impact of stellar feedback is evident: it is possible to identify two regions of star formation where stellar radiation disperses the cloud. This is particularly clear when looking at the H_2 and CO

[2] http://www.ita.uni-heidelberg.de/~dullemond/software/radmc-3d/
[3] https://home.strw.leidenuniv.nl/~moldata/

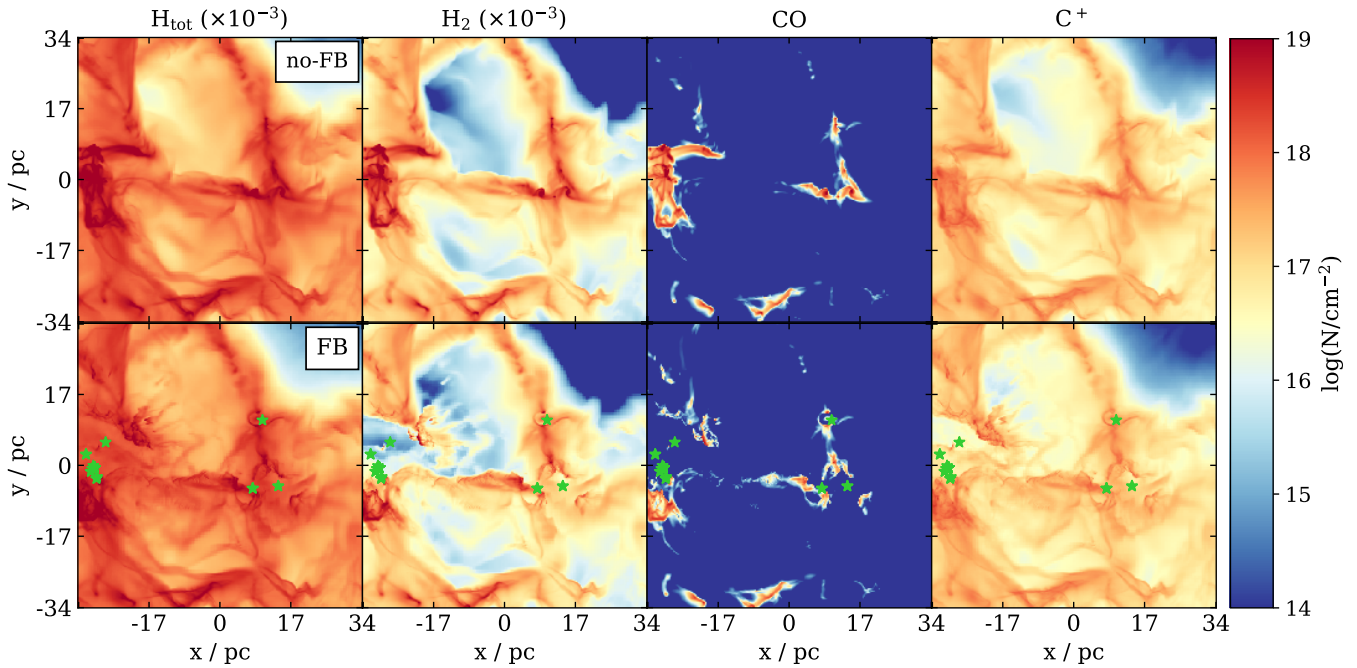

Figure 1. Column density of H_{tot}, H_2, CO, and C^+ (from left to right) of the run MC1-HD-noFB (top row) and MC1-HD-FB (bottom row) at t_{evol} = 4 Myr along the $z-$direction. Green symbols mark the positions where stars form. There is an evident nested CO - C^+ structure. The H_2 distribution is more diffuse than the CO distribution, which leads to a significant CO-dark H_2 region. Conversely, the C^+ distribution is significantly more diffuse than the H_2 distribution. The impact of stellar radiation is evident when comparing particularly dense regions in the noFB run with the corresponding areas in the FB run, as stellar feedback disperses the cloud.

maps, since the higher temperature and the stellar radiation lead to the dissociation of these molecules. Stellar radiation has also an impact on C^+ by further ionising it to C^{2+} (see Section 2.3). Furthermore, comparing the H_2 column density with the carbon-bearing species maps, shows that CO distribution is significantly more compact than the H_2 distribution, which leads to the presence of CO-dark H_2 regions (see Seifried et al. 2020, for details on this). The C^+ distribution is significantly more diffuse than the CO distribution, leading to a clearly visible nested CO−C^+ structure.

Fig. 2 shows the change in CO, C^+, and H_2 mass as a function of time for the simulated clouds in the zoom-in regions, using selected snapshots separated by 1 Myr in time. In our simulations, $M_{^{13}CO}$ (not shown here) is fixed to 1/69 of $M_{^{12}CO}$ (Wilson 1999). For runs without feedback, the CO abundance raises with time, and the C^+ abundance slowly decreases. The H_2 abundance also raises with time, even though at a lower rate than CO. Both the HD and MHD clouds follow the same trend, but the MHD clouds evolve more slowly: this can be seen, for instance, when considering the C^+-to-CO ratio (not shown explicitly in Fig. 2), which is much higher and more slowly decreasing in the MHD clouds than in the HD clouds. This is due to the inhibiting effect of the magnetic field on formation of dense structure and thus more H_2 and CO (Seifried et al. 2020). Stellar feedback reduces the amount of CO and H_2 from the onset of star formation. The total amount of C^+ is only marginally affected by stellar feedback (due to a partly conversion into C^{2+}), although feedback results in a different distribution of C^+ (see Fig. 1, right column).

3.2 Synthetic emission maps

Next, we analyse the emission maps for the same snapshots as in Fig. 2. In Fig. 3 we show the integrated intensity maps of the ^{12}CO, ^{13}CO, and [CII] lines of MC1-HD-noFB (top row) and MC1-HD-FB (bottom row) at t_{evol} = 4 Myr, which corresponds to the column density maps shown in Fig. 1. Again, a nested CO - [CII] structure is evident, and stellar feedback removes the CO emission from the expanding bubbles and strongly increases the [CII] emission, in particular from the rims of the bubbles.

Next, we calculate the total luminosity L. For this, we first sum the intensity of all pixels to obtain the integrated intensity. Then, L is given by

$$L = 4\pi d^2 F \,, \tag{16}$$

where d is the distance of the cloud and F is the total flux derived from the integrated intensity map by adding up the contributions from the total number of pixels, n:

$$F = \sum_{i=1}^{n} I_i \, A_{\rm pixel} \,. \tag{17}$$

Here, $A_{\rm pixel}$ is the area of the pixels in steradians given by

$$A_{\rm pixel} = \left(\arctan\left(\frac{a}{d}\right)\right)^2 \,, \tag{18}$$

with a being the side length of the pixel. We note that, due to the small angle approximation, for $a/d \ll 1$ the choice of d is practically irrelevant.

We show the values of L calculated for the three different LOS in Fig. 4. Optical thickness plays an important role for $L_{^{12}CO}$, indicated by the fact that the values for the same cloud, but different LOS, differ by up to a factor of a few, whereas in the optically thin case they should be identical. This is also shown by the fact that changes in M_{CO} (Fig. 2) are not directly reflected in corresponding changes in $L_{^{12}CO}$ (e.g. for MC1-HD-noFB). Conversely, the measured $L_{^{13}CO}$ is less affected by optical thickness: the difference in luminosity for the

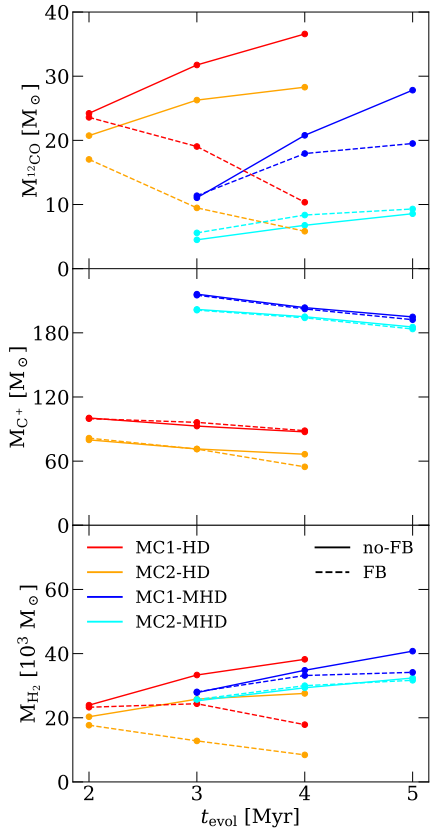

Figure 2. Mass of ^{12}CO, C$^+$, and H_2 (from top to bottom) as a function of time for all four clouds, represented in different colors. The noFB runs are plotted with solid lines, and FB runs in dashed lines. The CO mass raises with time, whereas the C$^+$ mass slowly decreases. HD and MHD clouds show the same trend, but the increase (for noFB runs) of H_2 and CO is slowed down in MHD runs with respect to HD runs. Stellar feedback disperses the densest parts of the clouds, where stars form, thus decreasing the mass of CO and H_2 over time.

different LOS is lower than for ^{12}CO, and $L_{^{13}CO}$ changes coherently with M_{CO}.

Stellar feedback significantly increases $L_{[CII]}$ compared to the noFB runs by a factor of 2 – 7. Only MC2-MHD-FB, which forms the least stellar mass among the clouds we investigate, does not show a significant increase in $L_{[CII]}$. In contrast, M_{C^+} is practically unchanged between noFB and FB runs (Fig. 2, middle panel). The increase in $L_{[CII]}$ is a consequence of the stellar radiation, which heats up the gas and excites the C$^+$ ions: we find that the excitation temperature of [CII] is overall significantly higher in FB than in noFB runs. In consequence, $L_{[CII]}$ increases for the FB runs despite a comparable amount of C$^+$ mass. Most of the [CII] luminosity in these runs comes from the rims of the HII bubbles, as shown for instance in Fig. 3. Pineda et al. (2013, 2014) claim that 34 – 70 per cent of the [CII] emission is related to feedback. The factor of 2 – 7 which we observe for the increase of the [CII] luminosity corresponds to a contribution of 50 – 85 per cent due to the role of stellar feedback, in rough agreement with the estimate of the aforementioned authors. Moreover, we find that the longer star formation proceeds, the more [CII] increases, thus having an increasingly more important effect in $L_{[CII]}$.

3.3 Feedback-driven [CII] bubbles

As explained in Section 2.3, we need to post-process the chemical abundance of C$^+$ in our feedback runs in order to take into account further ionization of C$^+$ to C^{1+} etc. due to stellar feedback.

In Fig. 5 we show the importance of this post-processing step. The total [CII] luminosity decreases by up to 60 per cent if the C$^+$ within the HII regions is post-processed compared to the non-post-processed case. In general, differences are larger at later evolutionary stages, as the stellar mass and thus stellar radiation increase over time. Hence, the consideration of higher ionisation states of carbon is crucial to obtain accurate [CII] intensities stemming from HII regions.

In Fig. 6 we show some examples of [CII] bubbles (HII regions) at different evolutionary stages. Stars are superimposed and are characterized with different colors and size according to their age and temperature. In Fig. A1 we also show the emission maps of the same regions obtained without operating the post-processing described in Section 2.3. These exhibit a much higher emission coming from the inner regions supporting the importance of the post-processing. We find that there are structures becoming more evident after the post-processing. This is the case of pillars, which can be easily recognised in the maps of MC2-HD-FB.

We note that the size of the bubble has a positive correlation with the age $t_\star$ of the stars formed inside. Larger bubbles (corresponding to later evolutionary stages) also show a weaker [CII] emission inside them than smaller bubbles (earlier stages).

We also observe a correlation between the star temperature and the size of the bubble. For example, the region around the rather cool star on the top of the map for MC1-HD-FB has still some [CII] emission, whereas the regions in the upper part of the maps of MC2-HD-FB and in the centre of MC2-MHD-FB are almost devoid of any emission despite comparable $t_\star$. Here $T_\star$ is significantly higher, i.e. the star is able to further ionise C$^+$.

At the rims of the bubbles, the [CII] emission is enhanced, when compared to even the brightest regions of the no-FB runs (Fig. 3). We emphasise that our findings are in excellent agreement with [CII] bubbles with enhanced emission at the rims and a lack of emission inside found recently in a number of observations (see e.g. Pabst et al. 2019; Luisi et al. 2021; Tiwari 2021). We plan to further investigate this strong prevalence of luminosity in the rims of the bubbles, together with the dynamical properties of the gas in such structures, in an upcoming, dedicated study.

3.4 The X_{CO} and $X_{[CII]}$ factors

The X_{CO} factor has been widely studied in literature (see e.g. Scoville et al. 1987; Dame et al. 1993; Strong & Mattox 1996; Melchior et al. 2000; Lombardi et al. 2006; Nieten et al. 2006; Smith et al. 2012; Ripple et al. 2013; Bolatto et al. 2013). It is defined as

$$X_{CO} = \frac{N_{H_2}}{I_{^{12}CO}} , \tag{19}$$

where N_{H_2} is the H_2 column density, generally expressed in cm^{-2}, and $I_{^{12}CO}$ the line-integrated intensity, expressed in K km s^{-1}. Here we calculate X_{CO} as the average quantity over the entire cloud. It allows to assess the H_2 mass of a cloud, given the intensity of ^{12}CO (1 → 0) transition. The typical X_{CO} value for the Milky Way is 2×10^{20} cm^{-2} K^{-1} km^{-1} s (e.g. Bolatto et al. 2013). We analogously define the $X_{[CII]}$ factor as

$$X_{[CII]} = \frac{N_{H_2}}{I_{[CII]}} . \tag{20}$$

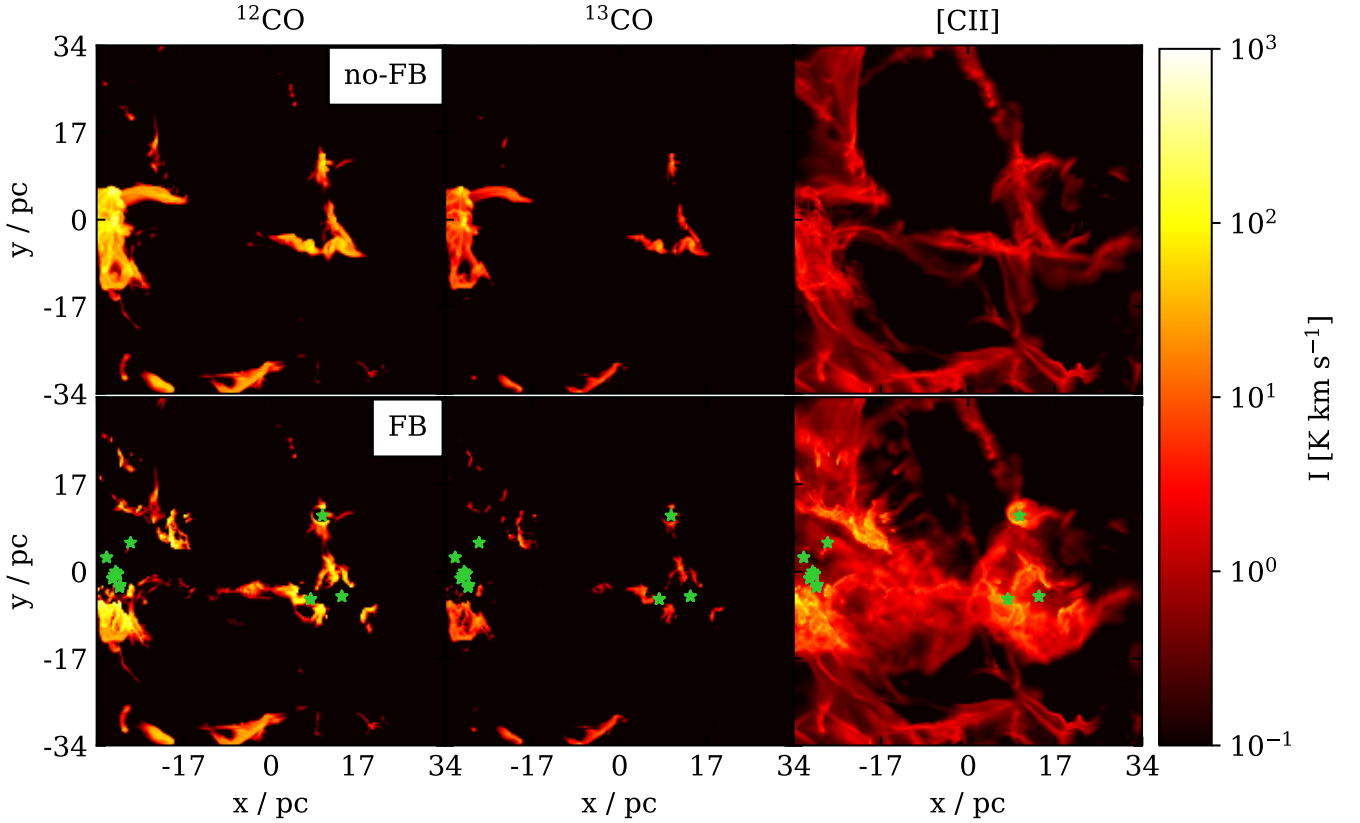

Figure 3. From left to right: integrated emission maps of ^{12}CO ($1 \rightarrow 0$), ^{13}CO ($1 \rightarrow 0$), and [CII] of MC1-HD without feedback (top row) and with feedback (bottom row) at $t_{\rm evol}$ = 4 Myr. The CMB background has been subtracted. A nested CO - [CII] is evident in both clouds. HII regions around stars devoid of any or most of the emission are visible in both the [CII] and in CO maps. [CII] intensity is enhanced by an order of magnitude in the rims of the HII regions with respect to the brightest areas in the non-feedback map.

In Fig. 7 we show both factors for our simulations plotted against the mass fraction of H_2 (see Seifried et al. 2020, for a plot against $t_{\rm evol}$). We calculate them under the assumption of unresolved clouds, i.e., we first integrate the H_2 column density and intensity over the entire area of the zoom-in regions, no matter whether in some pixels the intensity is beyond a minimum observable threshold, and then take the ratio of both values.

There is a significant scatter of $X_{\rm CO}$ (left panel of Fig. 7) around the reference value for the Milky Way. In our clouds it spans from ~ 0.5 to $\sim 4.5 \times 10^{20}$ cm^{-2} K^{-1} km^{-1} s. This scatter occurs among different clouds, but also to a smaller extent for the same clouds among different LOS and different $t_{\rm evol}$. It can in parts be attributed to the fact that a larger CO optical thickness leads to a higher $X_{\rm CO}$ factor, as the CO intensity does not increase coherently with the H_2 mass. Furthermore, differences occur between feedback and non-feedback runs, in particular for HD clouds. Stellar feedback lowers the $X_{\rm CO}$ factor, as it both slightly enhances the CO emissivity and reduces the H_2 mass (see Figs. 2 and 4).

Moreover, we cannot identify clear correlation between $X_{\rm CO}$ with the time evolution and the H_2 mass fraction of the clouds. We attribute this to the presence of "CO-dark" regions, i.e., molecular gas regions with low or no amount of CO. The amount of CO-dark gas is highly variable in different clouds. As discussed in more detail in Seifried et al. (2020), the CO-dark gas fractions in our MCs range from 40 to 95 per cent. Indeed, we find that the higher the CO-dark gas fraction, the higher is $X_{\rm CO}$, e.g. for MC1-HD-noFB and MC2-HD-noFB the CO-dark gas fraction is $\sim$ 40 per cent and $X_{\rm CO} = 1 - 2 \times 10^{20}$ cm^{-2} K^{-1} km^{-1} s, whereas for MC1-MHD-noFB and MC2-MHD-noFB the CO-dark gas fraction is 60 – 95 per cent, and the associated $X_{\rm CO}$ is $1.5 - 4 \times 10^{20}$ cm^{-2} K^{-1} km^{-1} s. We point out that the $X_{\rm CO}$ values calculated in Seifried et al. (2020) are slightly different, as there they were calculated considering only the pixel with a CO intensity above a minimum threshold of 0.1 K km s^{-1}.

The $X_{\rm [CII]}$ factor (right panel of Fig. 7) exhibits a lower scatter between the different LOS of the same cloud, which we attribute to the somewhat lower optical depths in the case of [CII]. Nevertheless, the scatter among different clouds is again significant, with $X_{\rm [CII]}$ values ranging from 0.5 to 12 $\times 10^{20}$ cm^{-2} K^{-1} km^{-1} s, which prevents us from using it as a reliable conversion factor to obtain the H_2 mass. This is in accordance with Franeck et al. (2018), where it is shown that most of the [CII] intensity comes indeed from atomic hydrogen gas, and not from molecular part. Hence, the monotonic increase in $X_{\rm [CII]}$ for the noFB runs is mainly due to the increase in H_2 mass, while the [CII] luminosity stemming from the outskirts of the clouds remains largely constant (see Figs. 2 and 4).

The FB runs, conversely, do not exhibit a clear relation because the stellar feedback both inhibits the formation of H_2 (Fig. 2) and enhances the [CII] intensity (Fig. 4).

3.5 The global CO/[CII] line ratio

The large scatter in $X_{\rm CO}$ makes it difficult to use it to reliably estimate the H_2 mass in a cloud. We therefore consider another pos-

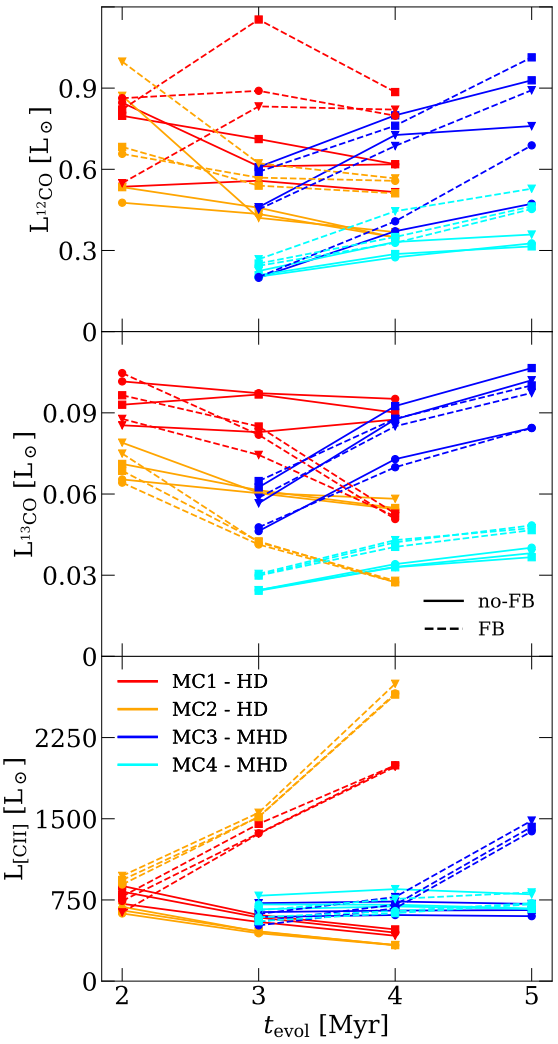

Figure 4. Total luminosity of ^{12}CO, ^{13}CO, and [CII] for the investigated clouds. Circles, squares, and triangles indicate values along $z-$, $y-$, and $x-$axis, respectively. The differences in the evolution of $L_{^{12}CO}$ and $L_{^{13}CO}$, together with the smaller scatter of $L_{^{13}CO}$ among the different LOS for the same cloud, indicate that ^{12}CO is more affected from optical thickness than ^{13}CO. The significant increase of $L_{[CII]}$ in the feedback runs is a consequence of the enhanced excitation temperature of C^+ due to stellar feedback.

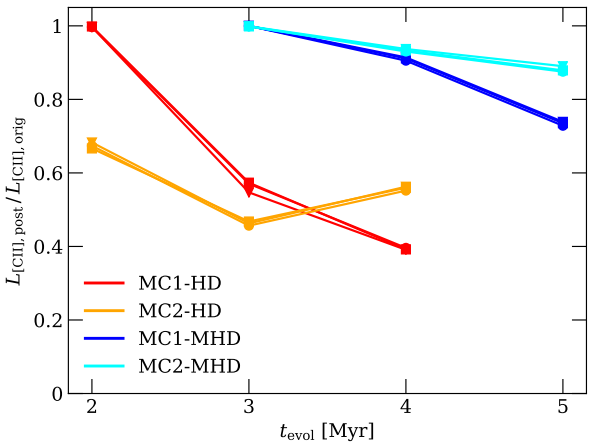

Figure 5. Ratio between the total luminosity of [CII] of the post-processed data, $L_{[CII],post}$, and the original data, $L_{[CII],orig}$. Circles, squares, and triangles indicate values along $z-$, $y-$, and $x-$axis, respectively. Post-processing the simulation data removes up to 60 per cent of the [CII] luminosity, especially at later stages where feedback becomes more important. Hence, it is essential to obtain reliable [CII] emission maps.

sible estimator: We take total luminosity, integrated over the entire cloud, $L_{^{12}CO}$, $L_{^{13}CO}$, and $L_{[CII]}$ and investigate the relation between $L_{^{12}CO}/L_{[CII]}$, $L_{^{13}CO}/L_{[CII]}$ and the H_2 mass fraction of the clouds, $M_{H_2}/M_{H,tot}$.

Fig. 8 shows $L_{^{12}CO}/L_{[CII]}$ and $L_{^{13}CO}/L_{[CII]}$ as a function of time (top row) and of the H_2 mass fraction $M_{H_2}/M_{H,tot}$ (bottom row). In the Appendix (Figs. A2 and A3) we also show the line ratios as a function of the H_2 mass and the [CII]/CO ratio calculated with luminosities given in units of erg s^{-1} cm^{-2} in order to allow for an easier comparison with observational literature. We note that we relate the luminosity ratio to the H_2 mass fraction rather than the H_2 mass, as the latter depends on the size of the cloud, i.e. it is an extensive quantity and not an intensive one as the mass fraction.

We find that different LOS of the same cloud typically have significantly different $L_{^{12}CO}/L_{[CII]}$ values with the exception of MC2-MHD (for both FB and noFB). The scatter is of a factor of a few in some snapshots: for instance, in MC2-HD-noFB at t_{evol} = 4 Myr, $L_{^{12}CO}/L_{[CII]}$ is ~1.5 for the LOS along the z-axis, but it is ~4.3 along the x-axis. Considering ^{13}CO instead of ^{12}CO considerably reduces the scatter. The same snapshot gives $L_{^{13}CO}/L_{[CII]}$ ≃0.4 along the z-axis and 0.5 along the x axis. As discussed, this is due to the smaller optical thickness of ^{13}CO (Borchert et al. 2021). Indeed, we would expect identical values for different LOS if the lines were optically thin. This is with good approximation the case for the snapshots which have very low CO column densities, i.e. MC2-MHD, which is a more diffuse cloud, and MC1-HD-FB and MC2-HD-FB at t_{evol} = 4 Myr (see Fig. 2), where stellar feedback has dispersed most of the dense regions.

We also observe a relevant scatter of a factor of up to a few in line ratios among different clouds for a selected H_2 mass fraction. This is a consequence of the different structures and properties of the clouds and does not change significantly when considering ^{12}CO or ^{13}CO. For instance, for $M_{H_2}/M_{H,tot} \simeq 0.3$, $L_{^{12}CO}/L_{[CII]}$ ranges from 2 to 6 and $L_{^{13}CO}/L_{[CII]}$ from 0.2 to 0.8. As we discuss in detail in the following, we do not observe a systematic relation between higher/lower line ratio values (at fixed H_2 mass fraction) and the presence/absence of magnetic fields or stellar feedback.

Stellar feedback has an impact on the evolution of the line ratio: if no feedback is considered, line ratio values increase with t_{evol}: this can be seen clearly for the HD runs, and, even though less evidently, also in the MHD runs. Conversely, including stellar feedback causes a decreasing ratio over time for the same clouds. This trend is less pronounced for MC2-MHD because it is less developed, and the stellar feedback has therefore a smaller impact.

Considering the luminosity ratios as a function of $M_{H_2}/M_{H,tot}$ shows an overall increasing relation for noFB runs (apart from optical thickness effects). Conversely, for the FB clouds, there is no clear trend any more. This is a consequence of the fact that both the H_2 mass fraction (Fig. 2) and the luminosity ratio (Fig. 8, left hand-side plot) decrease with t_{evol}, but with different slopes, making their reciprocal relation non-trivial.

In summary, there is no clear trend of the luminosity ratios with both t_{evol} and $M_{H_2}/M_{H,tot}$.

This implies that it is not possible to assess an age or evolutionary stage of a cloud by measuring a certain line ratio value.

Moreover, there is a large scatter among different LOS and different clouds. We refer to Section 4.1 for a further discussion about

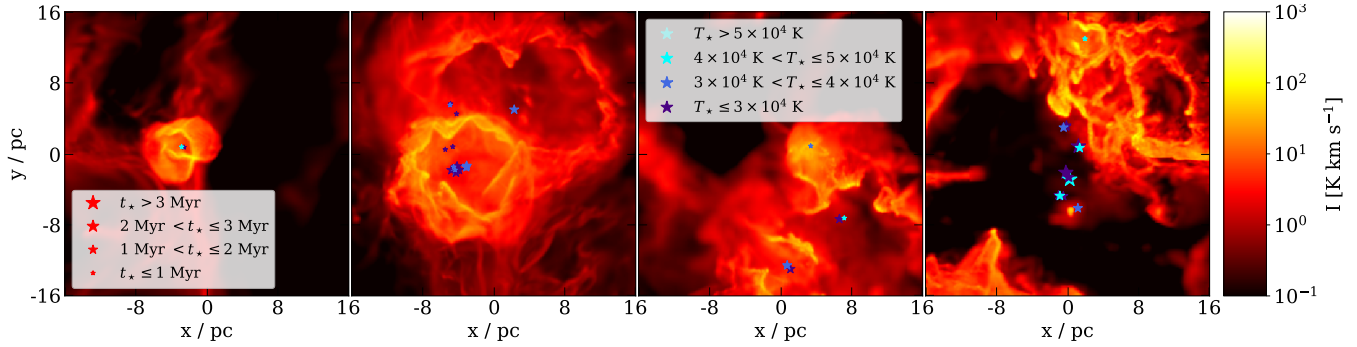

Figure 6. HII regions at different evolutionary stages as seen in [CII]. The individual snapshots are taken from different clouds: from left to right, i) MC2-MHD-FB, $t_{\rm evol}$ = 5 Myr, LOS along the $z-$axis; ii) MC1-MHD-FB, $t_{\rm evol}$ = 5 Myr, LOS along the $y-$axis; iii) MC1-HD-FB, $t_{\rm evol}$ = 4 Myr, LOS along the $y-$axis, and (iv) MC2-HD, $t_{\rm evol}$ = 4 Myr, LOS along the $x-$axis. The bubbles are ordered, from left to right, from the youngest to the oldest evolutionary stage. Stars formed are superimposed and plotted with different sizes and colors according to their age and temperature. We find than the largest and [CII]-darker bubbles are associated with older stars, whereas smaller and brighter bubbles correspond to younger stars.

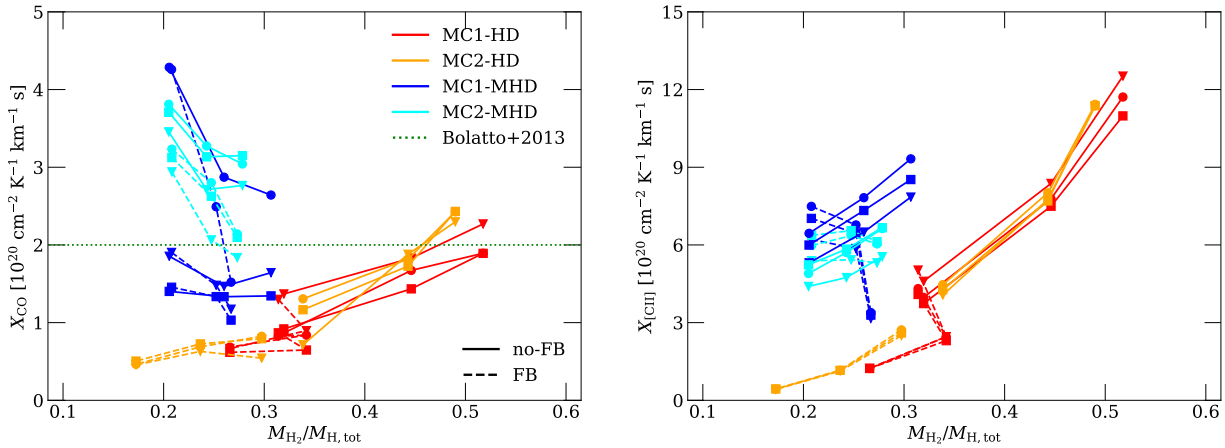

Figure 7. $X_{\rm CO}$ (left) and $X_{\rm [CII]}$ (right) of our simulated clouds as a function of the H_2 mass fraction. Circles, squares, and triangles indicate values along $z-$, $y-$, and $x-$axis, respectively. Regarding $X_{\rm CO}$, we find a significant scatter among the different clouds and in time around the reference value for the Milky Way of 2×10^{20} cm^{-2} K^{-1} km^{-1} s (dotted line). A similar scatter is found for $X_{\rm [CII]}$ as well. We see an increase of $X_{\rm [CII]}$ with $M_{\rm H_2}/M_{\rm H,tot}$ for the non-FB runs, wherease the FB runs show no clear trend.

the implications of these findings and a comparisons with recent observational works.

3.6 Analysis on single pixels

3.6.1 The intensity - column density relation

Next, we investigate – pixel by pixel – the relation between the intensity I integrated over the velocity channels of ^{12}CO, ^{13}CO and [CII] and the column density N of ^{12}CO, ^{13}CO, C^+, and H_2. This is shown in Fig. 9, where in the top row $I_{^{12}\rm CO}$ (left panel), $I_{^{13}\rm CO}$ (middle panel), and $I_{\rm [CII]}$ (right panel) are plotted as a function of $N_{\rm H_2}$. Each line represents the mean value of I for a given $N_{\rm H_2}$-bin for the selected snapshot. The bottom row shows the cumulative distribution of the intensity arising from regions with H_2 column densities lower or equal to the threshold of $N_{\rm H_2}$ given on the x-axis. Snapshots corresponding to different $t_{\rm evol}$ for the same cloud are plotted with the same color, and therefore are not distinguished here. We plot only the data resulting from the integration along the z-direction. However, we obtain qualitatively and quantitatively similar results when considering the x- or the y-direction. We note that the large scatter at very low and very high $N_{\rm H_2}$ is due to the low number of pixels in these regimes.

The column density at which $I_{^{12}\rm CO}$ and $I_{\rm [CII]}$ become optically thick is around $N_{\rm H_2} \simeq 10^{21}$ cm^{-2} in both cases. The $I_{^{13}\rm CO}$ values (middle panel of Fig. 9) show a similar behaviour, but the effect of optical thickness is less evident: deviations from optical thin behaviour occur at $N_{\rm H_2} \gtrsim 10^{21}$ cm^{-2}, but the change of slope is less pronounced than in the ^{12}CO case. The kink in the $I_{\rm [CII]}$ - $N_{\rm H_2}$ relation does not appear to happen for most of the FB runs. We attribute it to the fact that the regions, where $N_{\rm H_2} > 10^{21}$ cm^{-2}, are essentially the rims of the expanding bubbles (see Fig. 1). In these regions [CII] emission is enhanced by the effect of stellar radiation (see Section 3.3) and – even if optically thick – is thus larger than the intensity of a few K km s^{-1} coming from non-irradiated optically thick regions.

The values of $N_{\rm H_2}$ at which $I_{\rm CO}$ and $I_{\rm [CII]}$ become optically thick are in a good agreement, for instance, with the simulations of Bisbas et al. (2021), in particular regarding the $I_{^{12}\rm CO}$ - $N_{\rm H_2}$ relation, whereas the $I_{\rm [CII]}$ - $N_{\rm H_2}$ is more dependent on the environmental conditions of the simulated clouds. Moreover, Beuther et al. (2014) find an $I_{\rm [CII]}$ - N_{H_2} relation in the G48.66 cloud in good agreement with our curve, whereas a study of the Perseus Giant Molecular Cloud by Hall et al. (2020) shows an overall lower $I_{\rm [CII]}$ for given $N_{\rm H_2}$. Finally, comparing the $I_{^{12}\rm CO} - N_{\rm H_2}$ with the typical $X_{\rm CO}$ of

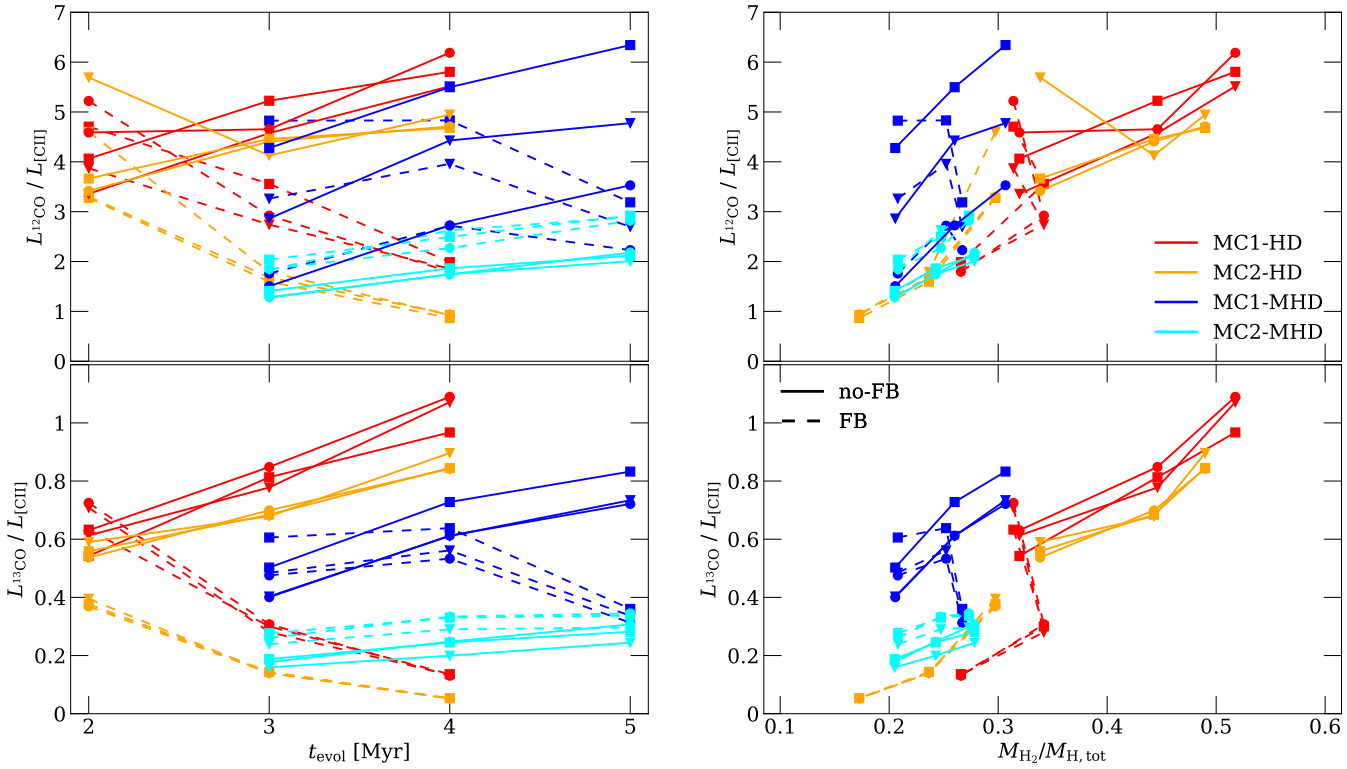

Figure 8. $L_{^{12}CO}/L_{[CII]}$ (top row) and $L_{^{13}CO}/L_{[CII]}$ (bottom row) as a function of t_{evol} (left column) and $M_{H_2}/M_{H_{tot}}$ (right column). For all no-FB runs the line ratio increases with t_{evol}. For all FB runs it decreases, with the only exception of MC2-MHD-FB, which has less dense gas. Altogether, there is no clear trend of the luminosity ratio with either t_{evol} and $M_{H_2}/M_{H,tot}$. In addition, there is a large scatter for a given evolutionary stage. The scatter among different LOS is reduced when considering ^{13}CO, due to its smaller optical thickness.

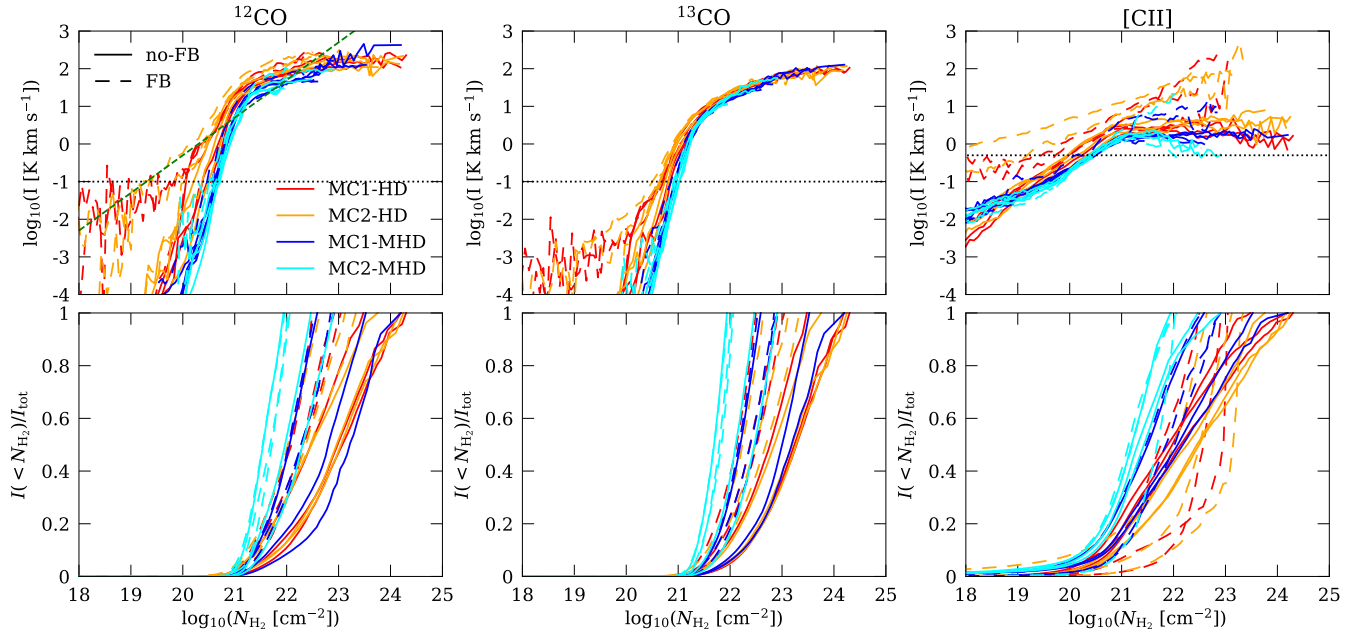

Figure 9. *Top row:* $I_{^{12}CO}$, $I_{^{13}CO}$, and $I_{[CII]}$ (from left to right) as a function of the column density of H_2 column density see along the z-axis. Lines (solid for no-FB runs and dashed for FB runs) represent the mean values for each N_{H_2}-bin. Snapshots at different t_{evol}, for a given cloud, are plotted with the same color. The dotted, horizontal lines represent realistic observable limits for CO and [CII], which we set to 0.1 and 0.5 K km s^{-1}, respectively. The dashed, green line in the top-left panel represents the X_{CO} reference value given by Bolatto et al. (2013). Optical thickness effects play a role for $N_{H_2} \gtrsim 10^{21}$ cm^{-2}. *Bottom row:* cumulative distribution of the intensity of ^{12}CO, ^{13}CO, and [CII] (from left to right) as a function of a N_{H_2} threshold value. Regions with $N_{H_2} < 10^{21}$ cm^{-2} are associated with a negligible CO emission, but they correspond to 5 - 20 per cent of the [CII] emission. The role of feedback is evident in MC1-HD and MC2-HD, where the most of [CII] emission comes from regions with $N_{H_2} > 10^{22}$ cm^{-2}, corresponding to the rims of the bubbles.

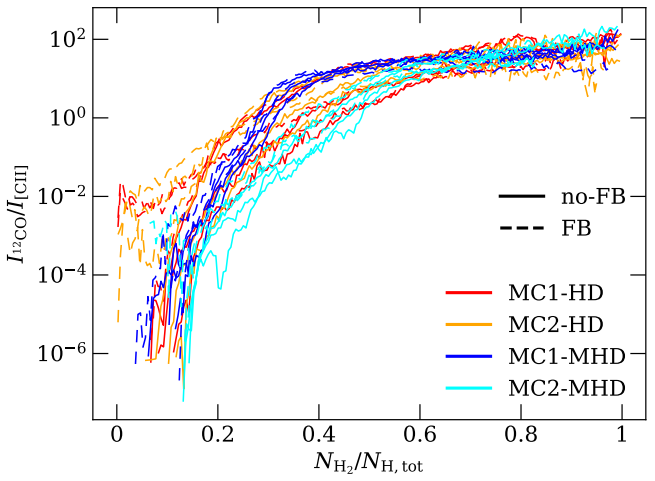

Figure 10. CO/[CII] intensity ratio plotted as a function of the H_2 mass fraction $N_{H_2}/N_{H,tot}$. We plot the snapshots at different t_{evol} with the same color. The line ratio increases with $N_{H_2}/N_{H,tot}$, although there is a large scatter, which is particularly relevant at high $N_{H_2}/N_{H,tot}$ as the relation is much shallower in this regime than at lower mass fraction. This prevents the usage of $I_{^{12}CO}/I_{[CII]}$ to determine $N_{H_2}/N_{H,tot}$.

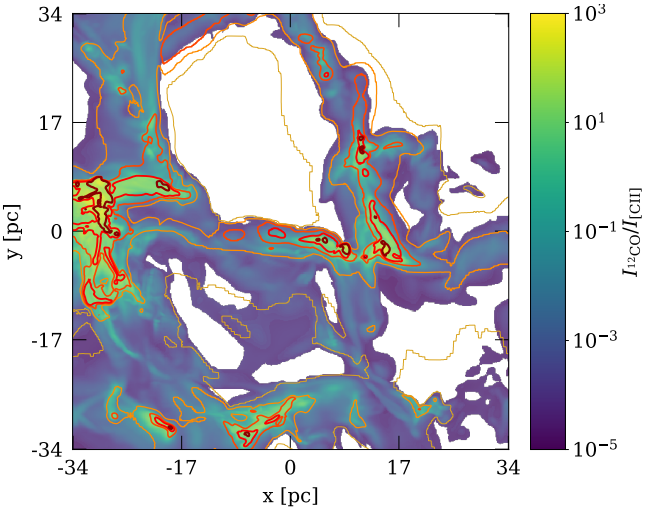

Figure 11. Map of $I_{^{12}CO}/I_{[CII]}$ for MC1-HD at t_{evol} = 4 Myr. Contour lines indicate an H_2 mass fraction $N_{H_2}/N_{H,tot}$ of 0.1, 0.3, 0.5, 0.7 and 0.9, respectively. We note a general correspondence between higher intensity ratio and higher $N_{H_2}/N_{H,tot}$ values. There are, however, significant differences in the line ratio for a given $N_{H_2}/N_{H,tot}$ value, especially in moderate $N_{H_2}/N_{H,tot}$ regimes.

$N_{H_2}/I_{^{12}CO} = 2 \times 10^{20}$ cm^{-2} K^{-1} km^{-1} (Bolatto et al. 2013, green line) shows that a linear relation between the two quantities does not hold on local scales, as already pointed out in Seifried et al. (2020).

In Fig. 4 we have already shown that the [CII] luminosity is enhanced by stellar feedback. Next, we analyse the column density regimes where the majority of luminosity comes from. For $N_{H_2} \geq 10^{22}$ cm^{-2} we report typical $I_{[CII]}$ values of 1 - 10 K km s^{-1} for no-FB runs and up to a few $\sim 10^2$ K km s^{-1} for feedback runs (right panel of Fig. 9). Stellar feedback causes an increase of the [CII] excitation temperature, that is, stronger emission for a given density. In general, areas with the highest N_{C^+} are those closer to the star-forming regions (see Fig. 1), therefore this is also the regime where difference between FB and no-FB runs are most evident. In addition, for the HD clouds (read and orange lines) at late evolutionary stages stellar feedback affects even larger parts of the clouds, such that the enhancement in $I_{[CII]}$ is visible also in lower column density regimes.

The cumulative distribution of the intensity (bottom row of Fig. 9) reveals the column density range from which the line emission comes from. We have no CO emission regions with $N_{H_2} < 10^{21}$ cm^{-2}, whereas 5 - 20 per cent of the [CII] emission comes from these areas. In general, the lines of the different clouds differ as each cloud has a different maximum N_{H_2} value. The role of feedback on the [CII] emission is particularly evident: a large part of the emission comes from the rims of the bubbles, which are dense regions. This is reflected in the steep ascent of the corresponding curves at $N_{H_2} > 10^{22}$ cm^{-2} for MC1-HD-FB and MC2-HD-FB, the clouds which are most affected by stellar feedback.

3.6.2 I_{CO} / $I_{[CII]}$ and H_2 mass fraction

In Section 3.5 we showed that there is no clear relation between the CO/[CII] luminosity ratio and the H_2 mass fraction. Now, we consider the intensity ratio $I_{^{12}CO}/I_{[CII]}$ as a function of $N_{H_2}/N_{H,tot}$ for each pixel of our maps. We need to be sure that we consider the same portion of the cloud for both for CO and C^+. For this purpose, we loop over the 201 velocity channels of our maps and indicate with $\{k\}$ the set of channels for which both specific intensities $I_{v,k,^{12}CO}$ and $I_{v,k,[CII]}$ are above specific intensity of the Cosmic Microwave Background (Eq. 15). We define

$$I_{^{12}CO} = \sum_k I_{v,k,^{12}CO} \Delta v \,, \tag{21}$$

where Δv is the width of a velocity channel, $I_{[CII]}$ is obtained analogously.

The result is shown in Fig. 10, where the mean values of the distribution of $I_{CO}/I_{[CII]}$ for a given N_{H_2} are shown using again the same color for snapshots referring to different t_{evol}. We show here the data referring to the LOS along the z-axis, but we obtain analogous results for the integration along the other LOS. The $I_{^{12}CO}/I_{[CII]}$ ratio increases with increasing $N_{H_2}/N_{H,tot}$. However, different clouds and snapshots show significantly different line ratios for given $N_{H_2}/N_{H,tot}$ with a typical scatter of up to 2 orders of magnitude. At very low values of $N_{H_2}/N_{H,tot}$ the scatter is even larger due to the low statistics. Furthermore, the presence of CO-dark and CO-bright pixels for the same N_{H_2} (as shown in detail in Seifried et al. 2020, see their figure 8) also contributes to enlarge such scatter.

Hence, the variability for a given $N_{H_2}/N_{H,tot}$ value is so large that the ratio $I_{^{12}CO}/I_{[CII]}$ cannot be reliably used to determine $N_{H_2}/N_{H,tot}$. This is also shown in the example given if Fig. 11, where we show a map of $I_{^{12}CO}/I_{[CII]}$ for MC1-HD-noFB at t_{evol} = 4 Myr. We overplot isocontour lines corresponding to H_2 mass fractions of 0.1, 0.3, 0.5, 0.7, and 0.9. There is a general correspondence between high line ratios and high H_2 mass fractions, but there are still significant variations in the line ratio within regions of similar mass fraction, especially for moderate mass fraction regimes.

Our results for the *pixel-by-pixel* approach are thus similar to that for the global luminosity ratio shown in Fig. 8, which also does not allow for a determination of the global H_2 mass fraction. However, we cannot directly compare the relation between $I_{^{12}CO}/I_{[CII]}$ and $N_{H_2}/N_{H,tot}$ with the one between $L_{^{12}CO}/L_{[CII]}$ and $M_{H_2}/M_{H,tot}$. For the pixel-by-pixel approach we also find H_2 column density fractions close to 0 and 1 and corresponding $I_{^{12}CO}/I_{[CII]}$ values spanning 8 orders of magnitude. On the other hand, the analysis of

$L_{^{12}CO}/L_{[CII]}$ representing unresolved clouds represents an average over the entire cloud and, as a consequence, both the mass fraction and the luminosity ratio span over a considerably lower range.

4 DISCUSSION

4.1 Intrinsic variability of line ratios

The ^{12}CO/[CII] and ^{13}CO/[CII] line ratios, shown in Fig. 8, are characterized by a large dispersion *alone* due to the difference in the structure and evolutionary stage of the clouds themselves, but not to different environments or external factors. In fact, all clouds form in a portion of a galactic disk with the same CRIR, G_0, and metallicity and with turbulence driven by supernovae. Furthermore, MHD runs have the same initial magnetic field strength. Despite that, $L_{^{12}CO}/L_{[CII]}$ varies by up to a factor of 5 for a given $M_{H_2}/M_{H,tot}$. The same applies when considering ^{13}CO, even though the scatter among different LOS for the same snapshot is reduced because of the lower optical thickness.

This scatter is also found in other works. For instance, Röllig et al. (2006) use the luminosity ratio to assess the environmental conditions like the cloud metallicity, density, and FUV field intensity[4].

Their models also exhibit large difference in the line ratio up to a factor of a few, even when leaving environmental conditions like the metallicity, FUV, and cloud density unchanged. Furthermore, also observational results at similar metallicities, e.g. for the LMC and 30 Doradus show a similar scatter of 5 - 10 in the [CII]/^{12}CO line ratio. In summary, as already stated by Röllig et al. (2006), we strongly disregard to use $L_{^{12}CO}/L_{[CII]}$ to infer physical properties of the clouds.

Furthermore, Madden et al. (2020) analyse the ^{12}CO and [CII] emission in a variety of environments. For normal galaxies and galactic star-forming regions, they find $L_{[CII]}/L_{^{12}CO} \approx 4000$, with a large scatter covering values from 300 to 25 000. Our simulation results are thus in good agreement with their findings, although they consider a much larger variety of environments.

Recently, Hall et al. (2020) analysed the ^{12}CO ($1 \rightarrow 0$) and [CII] emission from two regions of Perseus Giant Molecular Cloud. As their observations refer to a resolved portion of a cloud, this corresponds to our *pixel-by-pixel* analysis shown in Fig. 10. In general, we find that their reported values of $I_{^{12}CO}/I_{[CII]}$ of 2 – 100 agree well with ours. They also show that the highest values of the line ratio are reached where H_2 is more abundant, which is in agreement with our results.

Finally, Bisbas et al. (2021) analysed the line emission of several species from two different, simulated clouds with different environmental parameters. For comparable CRIR, G_0, and metallicity, they find ^{12}CO/[CII] line ratios larger by up to one order of magnitude compared to our work. We tentatively attribute this difference to two main factors. First, our clouds are somewhat more diffuse than the clouds used by Bisbas et al. (2021) (priv. communication). Indeed, when going to later evolutionary states, i.e. denser clouds, our line ratios increase (Fig. 8). Second, their work assumes chemical equilibrium, while we use non-equilibrium chemistry, a difference whose effects we will discuss in detail in the following.

[4] In order to compare values from observational works with our simulations, it might be necessary to convert the intensity from K km s^{-1} to erg s^{-1} cm^{-2} and recalculate the luminosity and luminosity ratio (see Fig. A3). Note that we plot [CII]/CO there, whereas Fig. 8 shows CO/[CII].

4.2 Equilibrium vs. Non-equilibrium chemistry

A large number of MC simulation works post-process their results to obtain chemical abundances by assuming that the chemical state is in equilibrium (see e.g. Gong et al. 2018; Li et al. 2018; Keating et al. 2020; Bisbas et al. 2021). As an example, Gong et al. (2020) study the X_{CO} factor for a wide range of environments. They evolve the chemical network for 50 Myr, i.e. equilibrium is roughly reached at that point, before analysing synthetic CO observations and the X_{CO} factor. However, the presence of phenomena like e.g. the turbulent mixing (see e.g. Glover & Mac Low 2007c; Valdivia et al. 2016; Seifried et al. 2017) suggests that this approach can determine inaccurate estimations at least for hydrogen and directly related quantities like e.g. X_{CO}.

Here, we aim to assess how much the assumption of equilibrium chemistry affects synthetic emission maps. In order to do so, we first select the snapshots of MC1-HD-noFB and MC2-HD-noFB at $t_{evol} = 2$ and 3 Myr and only evolve the chemistry for additional 120 Myr while the hydrodynamical state (total gas density, etc.) remains frozen. In the following, t_{chem} refers to the time for which the chemistry of the snapshot was evolved. We also define $M_{no-eq} = M(t_{chem} = 0)$ and $L_{no-eq} = L(t_{chem} = 0)$.

Fig. 12 shows the evolution of H_2, H, H^+, CO, C^+, and e^- as a function of t_{chem}. The CO and H_2 masses (left column) increase with t_{chem} by up to 30 and 120 per cent, respectively, in rough agreement with e.g. Gong et al. (2018). The masses of H^+ and e^- (right column) also increase over time but the increase is less pronounced (between 3 and 12 per cent).

The masses of C^+ and H decrease with t_{chem} by 7 and 60 per cent, respectively. In summary, these results once again confirm that the assumption of chemical equilibrium is – in particular for hydrogen-bearing species – questionable (Glover & Mac Low 2007c; Valdivia et al. 2016; Seifried et al. 2017; Seifried et al. 2022; Hu et al. 2021).

Furthermore, we find that CO and C^+ reach equilibrium at $t_{chem} \sim 10$ Myr, whereas H_2, H, and H^+ reach it after $\gtrsim 40$ Myr. In all cases, however, we can assume that at $t_{chem} = 50$ Myr (used in the following) equilibrium is roughly reached, as the relative changes with respect to later times are $\lesssim 5$ per cent.

The changes in chemical abundances by up to 120 per cent also affect the synthetic emission maps. In Fig. 13 we show the difference in total luminosity between the equilibrium (defined here as the state at $t_{chem} = 50$ Myr) and non-equilibrium state ($t_{chem} = 0$) for ^{12}CO and [CII]. The luminosity of CO increases in equilibrium by up to 50 per cent with respect to the non-equilibrium case. This increase is only marginally larger than the increase of CO mass (up to 30 per cent), indicating that the increase in M_{CO} itself is responsible for this luminosity change. Furthermore, due to the different gain in M_{H_2} (top left panel of Fig. 12) and L_{CO}, the value of X_{CO} determined at equilibrium is about 50 per cent larger than the actual value for the non-equilibrium state. However, this deviation is within the typical scatter of X_{CO} of a factor of a few found here (see Section 3.4) as well as in Gong et al. (2020) using equilibrium chemistry. Hence, differences caused by the equilibrium approach can hardly be assessed by comparing the values for X_{CO} obtained in both works.

On the other hand, the change in [CII] luminosity (right panel of Fig. 13) is considerably larger than the corresponding change in mass (as shown in Fig. 12), e.g. for MC1-HD-noFB at 2 Myr for one LOS we have $\Delta L/L_{non-eq} \simeq -30$ per cent compared to $\Delta M/M_{non-eq} \simeq -7$ per cent.

One element contributing to explain the difference between mass and luminosity change are the collisional partners, which in our case are H_2, H, and electrons. Focusing on H_2 and H, we find that the

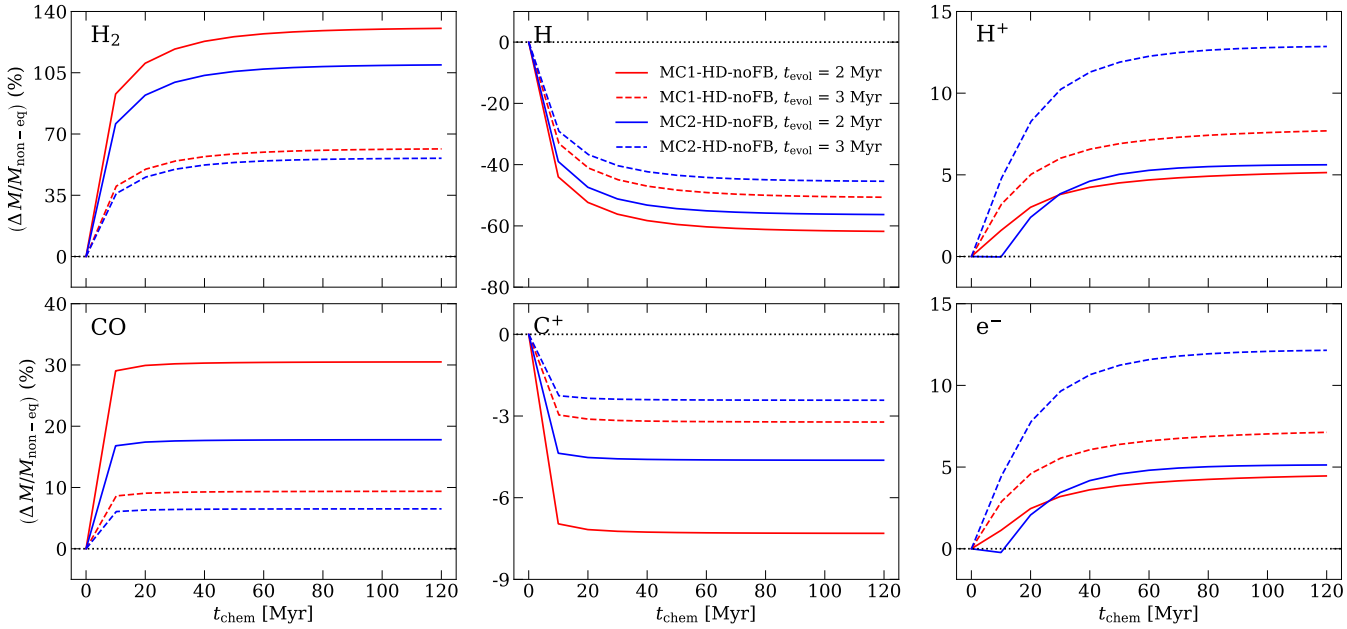

Figure 12. Relative mass variations of H_2, H, H^+, CO, C^+, and e^- (from top left to bottom right) for a selection of snapshots, obtained by freezing the evolution of the physics in the simulation and only evolving the chemistry for a time $t_{\rm chem}$. CO and C^+ reach equilibrium after $\sim$ 10 Myr, whereas H and H_2 reach equilibrium at $\gtrsim$ 40 Myr. The mass variations at equilibrium are particularly important for H (decreasing by up to 60 per cent) and for H_2 (increasing by up to 120 per cent), making the assumption of equilibrium for these species questionable. Variations for carbon-bearing species, H^+, and e^- are smaller.

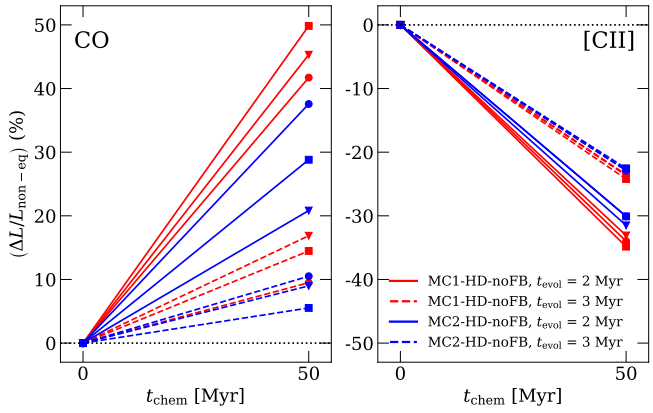

Figure 13. Relative luminosity variations of $L_{\rm CO}$ (left) and $L_{\rm [CII]}$ (right) between $t_{\rm chem}$ = 0 and $t_{\rm chem}$ = 50 Myr for the same selection of snapshot as in Fig. 12. The three different LOS are indicated with different markers. We note that the decrease in luminosity for [CII] is up to $\sim$ 30 per cent, while the corresponding decrease in mass only reaches $\sim$ 7 per cent. Changes in CO luminosity are comparable with the changes in CO mass.

first increases with $t_{\rm chem}$, whereas the latter decreases. Although the electron abundance increases for the equilibrium case and the $C^+ - e^-$ collisional rates are in general larger than those of H and H_2, this does not lead to an increase in $L_{\rm [CII]}$. We attribute this to the fact that the relative change of the electron abundance is significantly lower ($\lesssim$ 12 per cent) than for the other two collisional partners and the fact that there is little C^+ in the low-density/high-temperature regime, where the e^- collisional rates are high. Hence, as the [CII] emission is dominated by atomic gas (Franeck et al. 2018), the drop in H mass is mainly responsible for the drop in $L_{\rm [CII]}$.

The impact of the collisional partners effecting $L_{\rm [CII]}$ can also be expressed by the excitation temperature (see Fig. A4 in the appendix). We find that $T_{\rm ex}$ is overall lower for the equilibrium case. This thus contributes the larger decrease in luminosity than in mass when moving to equilibrium for C^+.

Another factor explaining why the relative changes of mass and luminosity for C^+ do not directly correspond is connected to the detailed distribution of C^+ in the density – temperature phase space. The majority of C^+ mass is contained in the Warm Neutral Medium (WNM), where the C^+ abundance is already quite close to chemical equilibrium. Evolving the chemistry to equilibrium does thus not imply a major change in this region and then the overall change in M_{C^+} is rather moderate. However, for observations towards MCs, the C^+ in the WNM – despite existing in its environement – contributes only little to the total [CII] luminosity. Rather, most of the luminosity comes from the Cold Neutral Medium (CNM) (Franeck et al. 2018). In the CNM, however, the C^+ abundance is further away from equilibrium, hence evolving the chemistry to equilibrium produces a significant change in the C^+ mass in this region, and in consequence on the total [CII] luminosity. The total change in C^+ mass (being dominated by the WNM) is, however, minor.

We emphasise that the values for $t_{\rm evol}$ = 2 Myr (solid lines in Figs. 12 and 13) change more both in term of mass and luminosity than the values for $t_{\rm evol}$ = 3 Myr (dashed lines). Hence, early evolutionary stages appear to be further away from a chemical equilibrium state, as the overall densities are still lower and thus chemical timescales longer. We thus argue that chemically post-processing MC simulations to equilibrium, in particular at an early evolutionary state, is questionable and should be considered with great caution.

Given the luminosity changes shown in Fig. 13, values for the $L_{\rm CO}/L_{\rm [CII]}$ ratio (not shown) increase by up to 100 per cent for the equilibrium case with respect to the non-equilibrium case. Assuming chemical equilibrium can therefore lead to a relative error of up to a factor of $\sim$ 2 when calculating such line ratios. As pointed out before, this error is generally larger at early evolutionary stages of the clouds. This effect can thus contribute to the differences seen in line ratios when compared to e.g. the work of Bisbas et al. (2021).

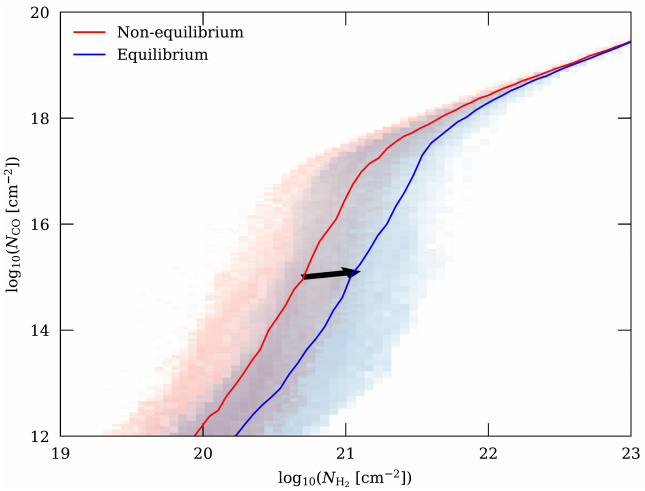

Figure 14. N_{CO} as a function of N_{H_2} for MC2-HD at t_{evol} = 2 Myr, considering the chemical state in non-equilibrium (red) and at equilibrium (blue). Shaded areas represent the 2D-PDFs and solid lines represent the mean values. The change is due to the larger increase in the H_2 mass than in the CO mass when moving from non-equilibrium to equilibrium chemistry (120 per cent vs. 30 per cent for the considered snapshot). The black arrow qualitatively indicates the change of the abundances for this transition.

Finally, we investigate the change in the relation between N_{H_2} and N_{CO} assuming chemical equilibrium. In Fig. 14 we show an example for MC2-HD-noFB at t_{evol} = 2 Myr. The red-shaded area represents the 2D-PDF for the original, non-equilibrium snapshot, whereas the blue-shaded area represents the equilibrium case. The two lines indicate the mean values. We observe a shift towards higher N_{H_2} for a given N_{CO} for chemical equilibrium, which we mainly attribute to the more pronounced increase in M_{H_2} than in M_{CO} in case of chemical equilibrium (see Fig. 12). We note that this in excellent agreement with results of Hu et al. (2021), who find a similar difference in mass changes for H_2 and CO concerning equilibrium and non-equilibrium states.

To summarize, we consider it as crucial to use non-equilibrium chemistry to simulate the H/H_2 content of MCs. Because of this, using chemical equilibrium for simulated MCs should be considered with great caution, in particular at early evolutionary stages, as it can significantly effect both the masses and luminosites of the various species.

5 CONCLUSIONS

We present an analysis of the abundance and luminosity of ^{12}CO, ^{13}CO and C^+ for 8 simulated MCs within the SILCC-Zoom project (Seifried et al. 2017), in which the chemical network is evolved *on-the-fly*. In particular, we investigate two clouds with and two without magnetic fields under solar neighborhood conditions at different evolutionary stages. For each simulation we consider a reference case without stellar feedback and one including radiative stellar feedback. For this purpose, we have developed a novel post-processing routine (based on Cloudy) to account for higher ionisation states of carbon. We show that this post-processing is essential to obtain reliable [CII] emission maps in feedback-dominated regions.

Our conclusions can be summarised as follows:

- The [CII] emission maps of feedback runs show expanding HII regions/bubbles, largely devoid of C^+ and [CII] emission inside, but with significant emission at the rims. This is in good agreement with in recent [CII] surveys.
- We estimate that radiative stellar feedback increases the [CII] luminosity by $\sim 50-85$ per cent compared to the non-feedback case due to an enhancement of the excitation temperature.

The CO luminosity decreases by up to a factor of 3 at late evolutionary stages of the clouds due to the dispersal of dense regions.

- The line luminosity ratios $L_{^{12}CO}/L_{[CII]}$ and $L_{^{13}CO}/L_{[CII]}$, integrated over the entire maps, show an increase with increasing H_2 mass fraction in noFB runs, but no clear relation in FB runs. We obtain values for $L_{^{12}CO}/L_{[CII]}$ from 1 to 6 and for $L_{^{13}CO}/L_{[CII]}$ from 0.1 to 1.1. We argue that due to the large spread, these line ratios *cannot* be used as a reliable tracer of the cloud's H_2 mass fraction. Similarly, this spread makes it difficult to use them to assess environmental parameters like the CRIR, the IRSF, or the metallicity.
- A pixel-by-pixel analysis of $I_{^{12}CO}/I_{[CII]}$ as a function of $N_{H_2}/N_{H,tot}$ shows an increase of the ratio with $N_{H_2}/N_{H,tot}$. However, as for the total luminosity ratio, also here the scatter is so significant that $I_{^{12}CO}/I_{[CII]}$ cannot reliably be used to predict the fraction of H_2 along the LOS.
- Evolving the chemistry to equilibrium as done in various works results in significant differences in terms of species abundance with respect to a self-consistent non-equilibrium approach used *on-the-fly* during the simulation. Hence, in particular for early evolutionary stages an equilibrium approach is questionable. We find that for the equilibrium case H_2 masses increase and H masses decrease by up to a factor of about 2. The abundances of other species like CO, C^+ and electrons change by a few 10 per cent.
- Assuming chemical equilibrium also affects the inferred luminosities of CO and [CII], with relative changes of up to +50 and −30 per cent, respectively. These luminosity changes cause an overestimation of the $L_{CO}/L_{[CII]}$ line ratios by up to 100 per cent if equilibrium chemistry is assumed. Similarly, the X_{CO} factor would be overestimated by up to 50 per cent.
- In general, the X_{CO} factor ranges between 0.5 and 4.5×10^{20} cm^{-2} K^{-1} km^{-1} s, showing no clear trend with respect to time evolution or the H_2 mass fraction. Feedback runs in general have a lower X_{CO} than the corresponding non-feedback runs. The similarly defined $X_{[CII]}$ factor ranges between 0.5 and 12×10^{20} cm^{-2} K^{-1} km^{-1} s, also not showing a clear trend with evolutionary time and H_2 mass fraction.

In summary, we show that it is crucial to take into account the effects (i) of stellar radiation in further ionizing C^+ within HII regions, and (ii) an *on-the-fly*, non-equilibrium chemistry treatment to accurately model CO and [CII] line emission in simulated MCs. We thus strongly suggest to consider both effects for future and more detailed comparisons with observations (Ebagezio et al., in prep.).

ACKNOWLEDGEMENTS

SW gratefully acknowledges the European Research Council under the European Community's Framework Programme FP8 via the ERC Starting Grant RADFEEDBACK (project number 679852). SE, DS, SW and PCN further thank the Deutsche Forschungsgemeinschaft (DFG) for funding through the SFB 956 "The conditions and impact of star formation" (sub-projects C5 and C6). TN acknowledges support from the DFG under Germany's Excellence Strategy - EXC-2094 - 390783311 from the DFG Cluster of Excellence "ORIGINS". The software used in this work was in part developed by the DOE NNSA-ASC OASCR Flash Center at the University of Chicago. We

particularly thank the Regional Computing Center Cologne for providing the computational facilities for this project by hosting our supercomputing cluster "Odin".

REFERENCES

Abel N. P., Ferland G. J., Shaw G., van Hoof P. A. M., 2005, ApJS, 161, 65
Appleton P. N., et al., 2013, ApJ, 777, 66
Beck R., Wielebinski R., 2013,] 10.1007/978-94-007-5612-0_13, p. 641
Beuther H., et al., 2014, A&A, 571
Bisbas T. G., Tan J. C., Tanaka K. E. I., 2021, MNRAS, 502, 2701
Bolatto A. D., Wolfire M., Leroy A. K., 2013, ARAA, 51, 207
Borchert E. M. A., Walch S., Seifried D., Clarke S. D., Franeck A., Nürnberger P., 2021, arXiv e-prints, p. arXiv:2102.00778
Borchert E. M. A., Walch S., Seifried D., Clarke S. D., Franeck A., Nürnberger P. C., 2022, MNRAS, 510, 753
Bouchut F., C. K., K. W., 2007, Numerische Mathematik., 108
Cecchi-Pestellini C., Bodo E., Balakrishnan N., Dalgarno A., 2002, ApJ, 571, 1015
Clark P. C., Glover S. C. O., Klessen R. S., Bonnell I. A., 2012, MNRAS, 424, 2599
Dame T. M., Koper E., Israel F. P., Thaddeus P., 1993, ApJ, 418, 730
Dame T. M., Hartmann D., Thaddeus P., 2001, ApJ, 547, 792
Derigs D., Winters A. R., Gassner G. J., Walch S., 2016, Journal of Computational Physics, 317, 223
Derigs D., Winters A. R., Gassner G. J., Walch S., Bohm M., 2018, Journal of Computational Physics, 364, 420
Dobbs C. L., Pringle J. E., 2013, MNRAS, 432, 653
Dobbs C. L., et al., 2014, Protostars and Planets VI, pp 3–26
Draine B. T., 1978, ApJS, 36, 595
Dubey A., Reid L. B., Fisher R., 2008, Phys. Scr., 132
Dullemond C. P., Juhasz A., Pohl A., Sereshti F., Shetty R., Peters T., Commercon B., Flock M., 2012, Astrophysics Source Code Library
Federrath C., Banerjee R., Clark P. C., Klessen R. S., 2010, ApJ, 713, 269
Franeck A., et al., 2018, MNRAS, 481, 4277
Fryxell B., et al., 2000, ApJS, 131, 273
Gatto A., et al., 2015, MNRAS, 449, 1057
Girichidis P., et al., 2016, MNRAS, 456, 3432
Glover S. C. O., Clark P. C., 2016, MNRAS, 456, 3596
Glover S. C. O., Mac Low M.-M., 2007a, ApJS, 169, 239
Glover S. C. O., Mac Low M.-M., 2007b, ApJ, 659, 1317
Glover S. C. O., Mac Low M.-M., 2007c, ApJ, 659, 1317
Glover S. C. O., Mac Low M. M., 2011,] 10.1051/eas/1152023, 52, 147
Glover S. C. O., Federrath C., Mac Low M. M., Klessen R. S., 2010, MNRAS, 404, 2
Gong M., Ostriker E. C., Kim C.-G., 2018, ApJ, 858, 16
Gong M., Ostriker E. C., Kim C.-G., Kim J.-G., 2020, ApJ, 903
Grenier I. A., Casandjian J.-M., Terrier R., 2005, Science, 307, 1292
Habing H. J., 1968, Bull. Astron. Inst. Netherlands, 19, 421
Haid S., Walch S., Seifried D., Wünsch R., Dinnbier F., Naab T., 2019, MNRAS, 482, 4062
Hall K. P., Stanimirović S., Lee M.-Y., Wolfire M., Goldsmith P., 2020, ApJ, 899
Hu C.-Y., Naab T., Walch S., Glover S. C. O., Clark P. C., 2016, MNRAS, 458, 3528
Hu C.-Y., Naab T., Glover S. C. O., Walch S., Clark P. C., 2017, MNRAS, 471, 2151
Hu C.-Y., Sternberg A., van Dishoeck E. F., 2021, arXiv e-prints, p. arXiv:2103.03889
Ibáñez-Mejía J. C., Mac Low M.-M., Klessen R. S., Baczynski C., 2016, ApJ, 824, 41
Keating L. C., et al., 2020, MNRAS, 499, 837
Klessen R. S., Glover S. C. O., 2016, Saas-Fee Advanced Course, 43, 85
Lada E. A., Blitz L., 1988, ApJ, 326, L69
Lahén N., Naab T., Johansson P. H., Elmegreen B., Hu C.-Y., Walch S., Steinwandel U. P., Moster B. P., 2020, ApJ, 891, 2
Larson R. B., 1981, MNRAS, 194, 809
Lesaffre P., Pineau des Forêts G., Godard B., Guillard P., Boulanger F., Falgarone E., 2013, A&A, 550, A106
Li M., Ostriker J. P., Cen R., Bryan G. L., Naab T., 2015, ApJ, 814, 4
Li Q., Narayanan D., Davè R., Krumholz M. R., 2018, ApJ, 869, 73
Lombardi M., Alves J., Lada C. J., 2006, A&A, 454, 781
Luisi M., et al., 2021, Science Advances, 7, eabe9511
Madden S. C., et al., 2020, A&A, 643
Melchior A. L., Viallefond F., Guélin M., Neininger N., 2000, MNRAS, 312, L29
Nelson R. P., Langer W. D., 1997, ApJ, 482, 796
Nieten C., Neininger N., Guélin M., Ungerechts H., Lucas R., Berkhuijsen E. M., Beck R., Wielebinski R., 2006, A&A, 453, 459
Offner S. S. R., Bisbas T. G., Bell T. A., Viti S., 2014, MNRAS, 440, L81
Ossenkopf V., 1997, New Astron., 2, 365
Ossenkopf V., Röllig M., Neufeld D. A., Pilleri P., Lis D. C., Fuente A., van der Tak F. F. S., Bergin E., 2013, A&A, 550, A57
Pabst C., et al., 2019, Nature, 565, 618
Padoan P., Pan L., Haugbølle T., Nordlund Å., 2016, ApJ, 822, 11
Papadopoulos P. P., Thi W. F., Viti S., 2004, MNRAS, 351, 147
Pineda J. L., Langer W. D., Velusamy T., Goldsmith P. F., 2013, A&A, 554
Pineda J. L., Langer W. D., Goldsmith P. F., 2014, A&A, 570
Rachford B. L., et al., 2009, ApJS, 180, 125
Ripple F., Heyer M. H., Gutermuth R., Snell R. L., Brunt C. M., 2013, MNRAS, 431, 1296
Röllig M., Ossenkopf V., Jeyakumar S., Stutzki J., Sternberg A., 2006, A&A, 451, 917
Salpeter E. E., 1955, ApJ, 121, 161
Schöier F. L., van der Tak F. F. S., van Dishoeck E. F., Black J. H., 2005, A&A, 432, 369
Scoville N. Z., Solomon P. M., 1975, ApJ, 199, L105
Scoville N. Z., Yun M. S., Clemens D. P., Sanders D. B., Waller W. H., 1987, ApJS, 63, 821
Seifried D., Walch S., 2016, MNRAS, 459, L11
Seifried D., et al., 2017, MNRAS, 472, 4797
Seifried D., Walch S., Reissl S., Ibáñez-Mejía J. C., 2019, MNRAS, 482, 2697
Seifried D., Haid S., Walch S., Borchert E. M. A., Bisbas T. G., 2020, MNRAS, 492, 1465
Seifried D., Beuther H., Walch S., Syed J., Soler J. D., Girichidis P., Wünsch R., 2022, MNRAS, 512, 4765
Sembach K. R., Howk J. C., Ryans R. S. I., Keenan F. P., 2000, ApJ, 528, 310
Shetty R., Glover S. C., Dullemond C. P., Klessen R. S., 2011a, MNRAS, 412, 1686
Shetty R., Glover S. C., Dullemond C. P., Ostriker E. C., Harris A. I., Klessen R. S., 2011b, MNRAS, 415, 3253
Smith M. W. L., et al., 2012, ApJ, 756, 40
Smith R. J., Glover S. C. O., Clark P. C., Klessen R. S., Springel V., 2014a, MNRAS, 441, 1628
Smith R. J., Glover S. C. O., Clark P. C., Klessen R. S., Springel V., 2014b, MNRAS, 441, 1628
Smith R. J., Glover S. C. O., Klessen R. S., 2014c, MNRAS, 445, 2900
Smith R. J., et al., 2020, MNRAS, 492, 1594
Solomon P. M., Rivolo A. R., Barrett J., Yahil A., 1987, ApJ, 319, 730
Stacey G. J., Geis N., Genzel R., Lugten J. B., Poglitsch A., Sternberg A., Townes C. H., 1991, ApJ, 373, 423
Strong A. W., Mattox J. R., 1996, A&A, 308, L21
Sutherland R. S., Dopita M. A., 1993, ApJS, 88, 253
Tielens A. G. G. M., Hollenbach D., 1985, ApJ, 291, 722
Tiwari M., 2021, in American Astronomical Society Meeting Abstracts. p. 137.03
Valdivia V., Hennebelle P., Gérin M., Lesaffre P., 2016, A&A, 587, A76
Velusamy T., Langer W. D., 2014, A&A, 572, A45
Waagan K., 2009, J. Comput. Phys., 228
Walch S., et al., 2015, MNRAS, 454, 238
Walker K. M., Song L., Yang B. H., Groenenboom G. C., van der Avoird A., Naduvalath B., Forrey R. C., Stancil P. C., 2015, American Astr. Soc.
Wilson T. L., 1999, Reports on Progress in Physics, 62, 143
Wilson R. W., Jefferts K. B., Penzias A. A., 1970, ApJ, 161, L43

Wünsch R., Walch S., Dinnbier F., Whitworth A., 2018, MNRAS, 475, 3393
Wünsch R., Walch S., Dinnbier F., Seifried D., Haid S., Klepitko A., Whitworth A. P., Palouš J., 2021, MNRAS, 505, 3730
van Dishoeck E. F., Black J. H., 1988, ApJ, 334, 771

APPENDIX A: SUPPLEMENTARY FIGURES

In the following, we show some additional plots which help in clarifying several aspects of the paper. In Fig. A1 we show the same expanding bubbles as in Fig. 6, but now for the case with and without the post-processing for C^{2+} (see Section 2.3) to allow for a direct comparison. The importance of the post-processing in removing the [CII] intensity coming from the interior of the bubbles is evident, in particular for bubbles associated with older and hotter stars.

In Fig. A2 we show $L_{^{12}CO}/L_{[CII]}$ (left side) and $L_{^{13}CO}/L_{[CII]}$ (right side) as a function of the H_2 mass, instead of the H_2 mass fraction (see Fig. 8). The correspondence of the line ratio with the H_2 mass is even weaker than with the H_2 mass fraction. This is due to the fact that the mass is an extensive quantity, whereas line ratios and mass fractions are intensive quantities.

In Fig. A3 we show the line ratios using units of erg s^{-1} for the luminosity. This allows an easier comparison with some observational results e.g. by Röllig et al. (2006) (see Section 4.1).

In Fig. A4 we show a 2D-PDF of the gas temperature and the excitation temperature for MC1-HD-noFB at $t_{evol} = 2$ Myr. The upper plot refers to the non-equilibrium (i.e., $t_{chem} = 0$), and the bottom plot refer to the equilibrium state ($t_{chem} = 50$ Myr) as discussed in Section 4.2. Due to the changes in the collisional partners (see Fig. 12), the excitation temperature is lower at equilibrium, which explains why the [CII] luminosity decreases when evolving the chemistry to equilibrium.

This paper has been typeset from a TEX/LATEX file prepared by the author.

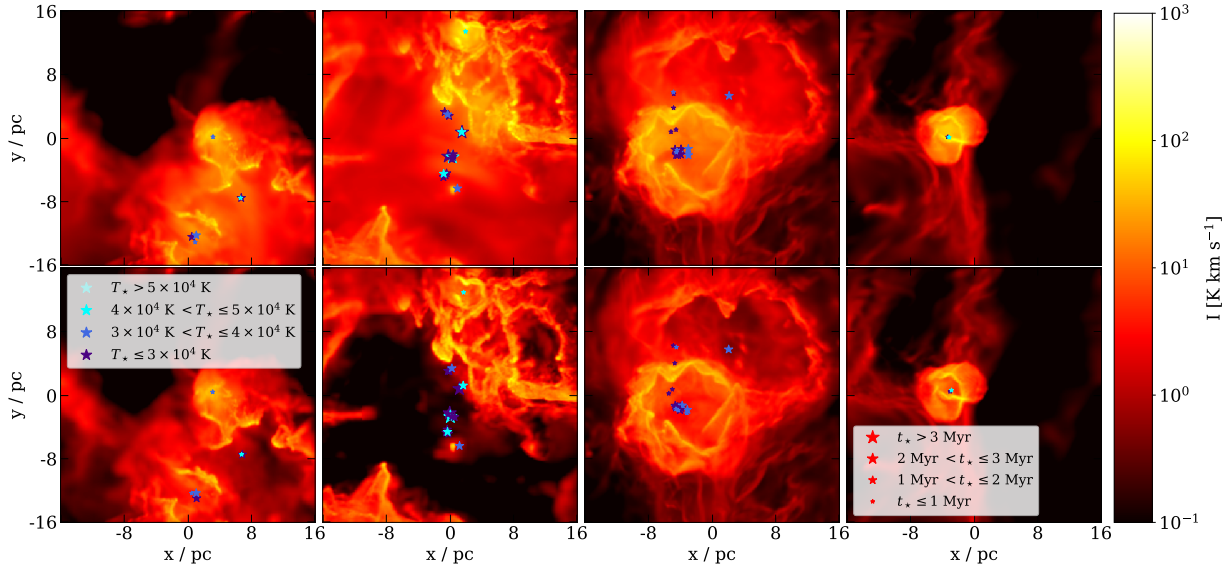

Figure A1. Examples of synthetic [CII] emission maps of expanding feedback bubbles, before (top row) and after the post-processing described in Section 2.3 to account for the conversion of C^+ into C^{2+} (bottom row). The importance of the post-processing in reducing the [CII] intensity coming from the interior of the bubbles is evident, in particular for bubbles associated with older and hotter stars.

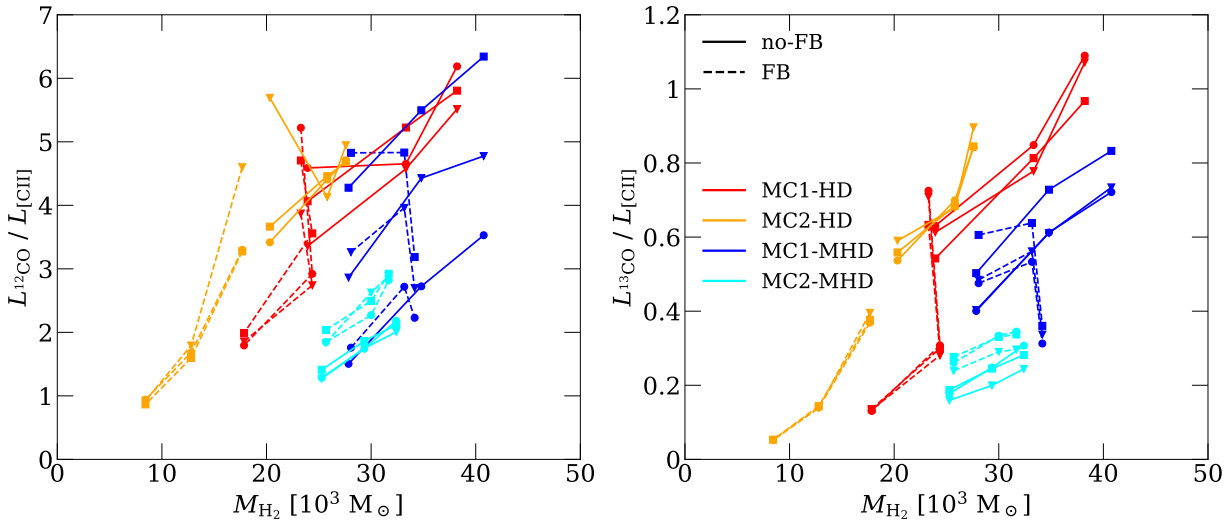

Figure A2. $L_{^{12}CO}/L_{[CII]}$ (left panel) and $L_{^{13}CO}/L_{[CII]}$ (right panel) as a function of the H_2 mass as opposed to Fig. 8 where it is plotted against $M_{H_2}/M_{H,tot}$. As the luminosity ratio is an intensive property of the clouds, while the H_2 mass is extensive, the relation shows an even larger scatter than the one against the H_2 mass fraction (see Fig. 8).

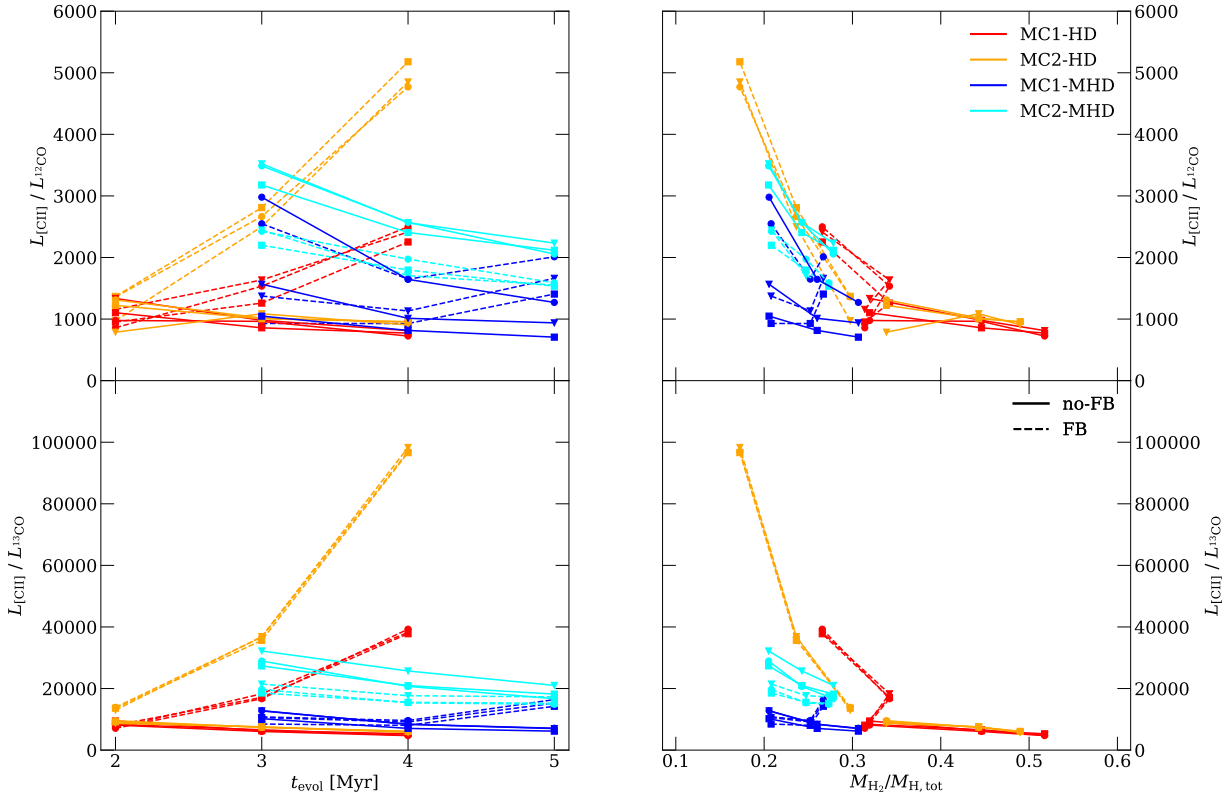

Figure A3. $L_{[CII]}/L_{^{12}CO}$ (top row) and $L_{[CII]}/L_{^{13}CO}$ (bottom row) as a function of t_{evol} (left column) and $M_{H_2}/M_{H_{tot}}$ (right column). Luminosities are expressed in erg s^{-1} as opposed to the usage of K km s^{-1} in the main body of the paper.

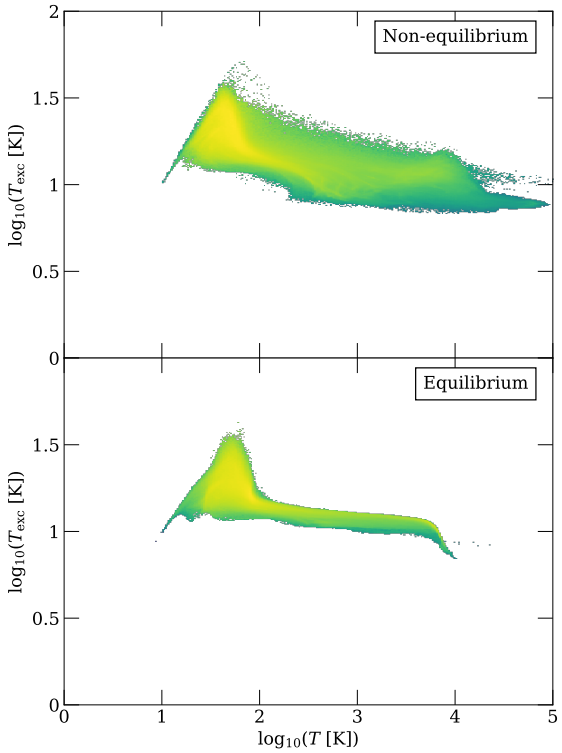

Figure A4. 2D-PDF of excitation temperature T_{ex} as a function of the gas temperature. The upper plot represents MC1-HD-noFB at t_{evol} = 2 Myr with the chemistry evolved *on-the-fly*, the bottom plot represents the same snapshot at steady state, i.e. at t_{chem} = 50 Myr.